Spatio-Temporal Optical Computing:
Its Concept and Applications
(空間光時間光コンピューティング：概念と応用)

2001, March

Yukihiro Ishii

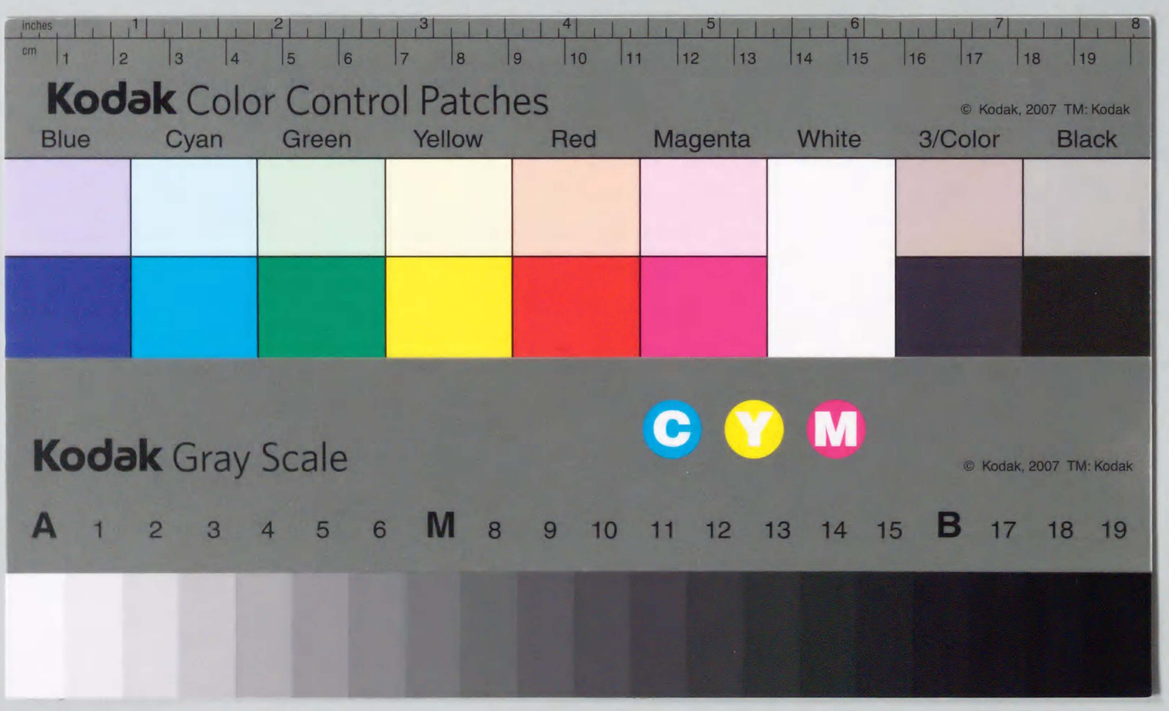

Spatio-Temporal Optical Computing: Its Concept and Applications

(時空間光情報処理: 概念と応用)

Doctoral Program in Engineering
University of Tsukuba
2001, March
Yoshiaki Yasuno

Spatio-Temporal Optical Computing: Its Concept and Applications

by

Yoshiaki Yasuno

Then Jesus said to them, little while longer the light is with you. Walk while you have the light, lest the darkness overtake you; he who walks in the darkness does not know where he is going. While you have the light, believe in the light, that you may become sons of light.

John 12:35–36

Abstract

The concept and applications of spatio-temporal optical computing are proposed. This concept introduces ordinary spatial optical computing techniques using Fraunhofer and Fresnel diffraction into time domain.

The concept is classified in three phases. The first phase employs spatio-temporal duality of light. In this thesis a new algorithm to analyze low coherence interferograms is proposed in this phase.

The second phase employs spatio-temporal conversion. In this phase we construct a femtosecond pulse separation measurement system which determines the pulse separation in the accuracy of 12.4 fs. Furthermore, by employing the conversion technique, a less scanning dimension and all optical spectral interferometric optical coherence system is constructed. This system determines the surface profiles of specular and rough surface samples.

The third phase employs spatio-temporal coupling effects. We numerically investigate on the spatio-temporal coupling behavior of light in a pulse shaper, spatio-temporal coupled pulse shaper and time-domain microscope by employing the spatio-temporal Wigner distribution function. Some conditions which induces the coupling are shown.

Contents

Chapter 1

Introduction

Large mount of techniques in the field of optical computing, employing the high spatial parallelism and high information-carrier-capability of light, have been studied. These optical computing techniques are classified to two large categories. One is non-diffractive, geometric optical computing, such as an optical neural network, and the other is diffractive versions, such as a joint transform correlator, matched filter, holograms. Almost all of the diffractive versions are based on the Fraunhofer diffraction[1], and pseudo Fraunhofer diffraction developed by a 2-f optical setup[1]. By the spatial Fourier transform, the spatial image is decomposed to its spatial spectral components and the components are spread spatially.

In the field of laser mode-locking techniques, many femtosecond pulse laser systems have been developed. Because some of them demand very easy operation and low economical cost, these lasers have been widely applied in many physical and industrial field, such as optical communication, industrial and biomedical measurement or ultrafast control of physical and chemical properties of materials. To achieve such applications, we have to control such ultrafast light pulses with high temporal accuracy. In most cases, the high accuracy-control is achieved by employing a spectral modulating pulse shaper[2, 3, 4, 5, 6]. The pulse shaper decomposes the temporal spectrum components of a ultrafast light pulse spatially by a grating-lens pair, modulates the spectrum, and then reconstructs a temporally modulated light pulse by another grating-lens pair[5].

These techniques in the two fields have theoretical relationships. Because the spatial and temporal behaviors of light are expressed by similar equations. Furthermore, both the two techniques employ the spatial or temporal optical Fourier transform.

In parallel with the progress of the optical computing and ultrafast optics, large numbers of optical measurement techniques have been studied. Optical profilometry techniques are classified in two large categories; one employs spatial signal processing, and the other employs temporal signal processing techniques. The spatial versions are represented by Fourier transform profilometry[7], project grating image methods[8], and large numbers of spatial interference fringe analysis techniques. The temporal versions are represented by low coherence or white light inteferometory, and optical coherence tomography[9, 10, 11]. By conventional classification, these methods are also classified in spatial version. However, we classify these techniques in spatial ver-

sion, because these techniques encodes the profile information of a test object in the temporal complex profile of light electric fields. Although the techniques are in spatial and temporal domains, all of the techniques have large analogies. Almost all these measurement techniques encode the profile of a test object by the phase modulation of a spatial or a temporal fringe. In spatial version, the fringe is an interference fringe, and in temporal version, the fringe is an interferogram.

Large numbers of fringe analyzing techniques have been proposed and most of them employ Fourier transform. Hence optical computing techniques can be applied to optical measurement, and some studies have been reported. But these studies are only for spatial optical measurement.

Based on the spatio-temporal analogy and duality, we explore the field of spatio-temporal optical computing. At first, we classify the spatio-temporal optical computing techniques into three phases.

The first phase is based on *spatio-temporal duality*. Spatial optical computing techniques are applied to temporal signals, and temporal signal processing techniques are applied to spatial images employing the spatio-temporal duality.

The second phase is based on the techniques of *spatio-temporal conversion* employing the spatio-temporal duality. Using the analogy between spatial optical computing techniques and a temporal ultrafast pulse shaper, we construct a time-to-space or space-to-time optical signal converter. We can treat optical temporal signals by a spatial optical computing system by using the converter, so that we can introduce the spatial optical computing techniques to time domain.

The third phase is based on spatio-temporal coupling phenomena. The spatial state of an electric field is not determined only by the ex- spatial state of the field but also the temporal one. Its temporal state is also determined as the same. The phenomenon is called *spatio-temporal coupling*. In conventional optical systems, such as a spectrometer or a pulse shaper, the spatio-temporal coupling is not desired, but unavoidable. We have intend to reduce the coupling effect. The spatio-temporal effect is unavoidable but easy to reduce. However, we can also apply the effect positively. In the third phase of spatio-temporal optical computing, we enhance the coupling effect and apply it actively.

In this thesis, we investigate the detail of the concept and applications of the spatio-temporal optical computing. In chapter 2, we propose a new signal processing algorithm to analyze low coherence interferograms, named a *phase-resolved correlation method* employing the spatio-temporal duality. The algorithm improves the sensitivity and the resolution of a low coherence interferometer.

In chapter 3, we construct a time-space converter, a *spatio-temporal joint transform correlator (ST-JTC)*, employing the spatio-temporal duality and the principle of a conventional spatial joint transform correlator[1] and a pulse-shaper[2, 3]. This system superimposes the temporal profile of a femtosecond pulse shape on a spatial plane.

In chapter 4, we invent an all optical, less scanning optical coherence tomography system, *spectral interferometric joint transform optical coherence tomography system (SIJT-OCT)* employing the principle of the spatio-temporal joint transform correlator. The system includes a super luminescent diode (SLD) light source, and determines the three-dimensional surface of a test object with one-dimensional mechanical scanning operation.

In chapters 5, 6, and 7, we investigate the spatio-temporal behavior of some optical systems in which the spatio-temporal coupling effects are occurred. In each chapter, a conventional pulse shaper, a spatio-temporally coupled pulse shaper (STCPS), and a time-domain microscope are investigated. The spatio-temporally coupled pulse shaper proposed by us is one of the improved pulse shapers to simultaneously control the spatial and temporal profile of an ultrafast light pulse by one-dimensional spatial light modulation employing enhanced spatio-temporal coupling.

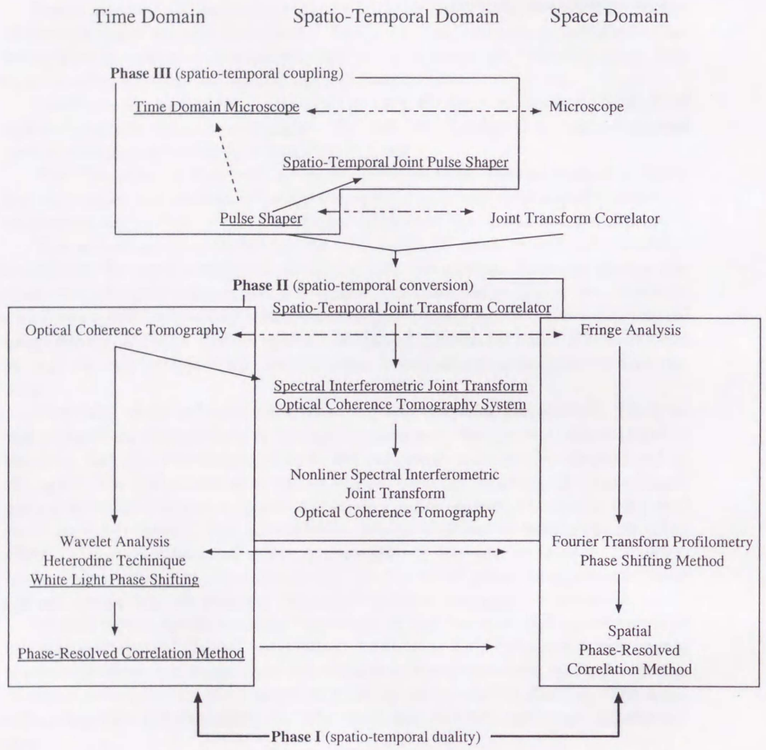

Figure 1.1: The relationship of spatio-temporal optical computing and measurement techniques.

Part I

Spatio-Temporal Duality

We find a number of dualities and analogies between the spatial and temporal properties of light. The Fresnel diffraction in space domain is very similar to linear dispersion in time domain[12], and interference fringes in space domain have some similar properties with an interferogram in time domain. By using the duality and analogies, many spatial signal processing techniques are applied to analyze temporal signals and many temporal techniques are applied to spatial signals.

In some case, such applying is, however, have less performance, because the spatial and temporal signals also have a few different properties. By understanding the difference precisely, and modifying the techniques, the application will have a good performance.

In this part, we propose a new signal processing algorithm, phase-resolved correlation algorithm. This algorithm is originally based on the spatial phase oriented fringe analysis techniques, such as Fourier transform profilometry[7] or phase shifting method[8], but modified to apply to the temporal interferogram.

Chapter 2

Phase-Resolved Correlation Method

In this chapter,a new signal processing technique is proposed, involving a phase-resolved correlation method which can be used to determine the phase distribution of low coherence interferograms. This method improves the sensitivity and selectivity of low coherence interferometers. The depth structure of an aluminum oxide coated aluminum mirror was determined using a low coherence interferometer by employing this method. Three signal peaks were successfully extracted from a noisy interferogram.

2.1 Introduction

A number of phase-oriented signal processing methods have been widely investigated for signals with carrier-frequency, including the use of moiré images, interference fringes and interferograms. The phase-shifting method and Fourier transform profilometry[7] are among the most commonly used methods applied to this kind of analysis, since they can extract the carrier-phase-distribution from a signal and thus improve its signal-to-noise ratio (SNR).

Non-destructive, high-sensitivity profilometry techniques, such as white light interferometry and optical coherence tomography (OCT) have been applied to various fields, including industrial processing and biomedical applications[13, 14, 9]. Many signal processing methods and advanced techniques for gaining better SNR of interferograms have been applied to interferometers[15, 10, 11]. However, phase-oriented signal processing methods have seldom been employed, although they clearly have potential for developing good SNR. The reason is that the phase shifting method demands carrier phase shifting with respect to its envelope. On the other hand, in most cases of interferogram analysis, Fourier transform profilometry does not give good results due to the model assumed for the interferogram. Fourier transform profilometry assumes that the analyzed signal has only one phase-modulated carrier, although in reality, an interferogram represents the sum of several independent signals, each with a different carrier phase.

We introduce a novel signal processing method for analyzing interferograms, based on phase-resolved correlation, in which a one-dimensional interferogram

is resolved into a three-dimensional intensity distribution in position-frequency-phase space. Each independent signal peak in one interferogram has a different carrier phase, allowing the signal peaks to be separated along the phase axis. Furthermore, this method can separate the important signals from background noise according to their frequency characteristics. In the following section, we will describe an experimental demonstration in which three peaks, otherwise masked by noise, are extracted from a low SNR interferogram.

2.2 Principle

We assume the analyzed signal to be $f(z)$. The phase-resolved correlation method separates the important signal and the noise in $f(z)$ by calculating the discrete correlation between a reference wavelet and the analyzed signal. The reference wavelet is assumed to be

$$h(z, \phi, \nu) = h_e(z) \times h_c(z, \phi, \nu) \tag{2.1}$$

where $h_e(z)$ is the envelope of the reference wavelet and $h_c(z, \phi, \nu)$, the carrier of the reference wavelet, are assumed to be

$$h_c(z, \phi, \nu) = \sin(2\pi\nu x + \phi) \tag{2.2}$$

where ν is the carrier frequency and ϕ is the phase-bias variable. For application to interferogram analysis, the envelope is assumed to be a Gaussian shape in

$$h_e(z) = \exp\left\{-\pi (x/\beta)^2\right\} \tag{2.3}$$

where β denotes the width of the envelope. The reason is that the temporal coherence function of a white light or low coherence light source is in most cases a Gaussian function.

The phase-resolved correlation function of $f(z)$ is defined as

$$W(n_z/\nu, \phi, \nu) = \int_{-\infty}^{+\infty} h(z - n_z/\nu, \phi, \nu) f(z)\, dz \tag{2.4}$$
$$\begin{cases} nz & : \cdots, -2, -1, 0, 1, 2, \cdots \\ \phi & : [-\pi, +\pi] \\ \nu & : [0, +\infty] \end{cases}$$

where n_z is an integer, making W a spatial discrete function whose spatial sampling period is $1/\nu$. The one-dimensional signal $f(z)$ is expressed as a three-dimensional, discrete-position, phase and frequency intensity distribution according to the correlation function.

Now we calculate the phase-resolved correlation of the signal shown in Fig. 2.1. In this case, to simplify the example, our investigation involves only one frequency. The carrier frequency of the signal is determined by its discrete Fourier-transformed spectrum. The important signals are localized near the carrier frequency, and so the two-dimensional correlation includes all the signals except for the noise. We use a Gaussian wavelet with a carrier frequency of 2.3×10^6 m^{-1} and width of β=7×10^{-9} as shown in Fig. 2.2. This algorithm which is implemented in programming language C on 800MHz PentiumIII processor takes

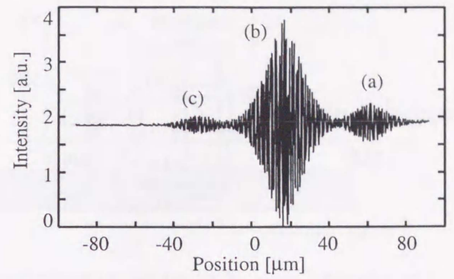

Figure 2.1: Analyzed fringe signal. Three peaks which have separate carrier-phases are present in the signal.

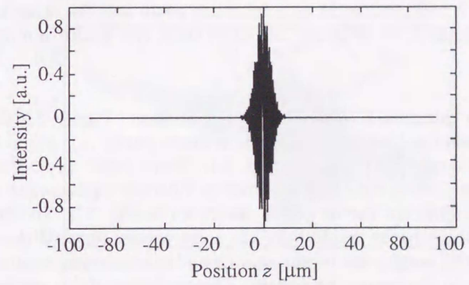

Figure 2.2: A reference wavelet for correlation. The envelope is a Gaussian function and its width is determined as the coherence length of the light source of the interferometer.

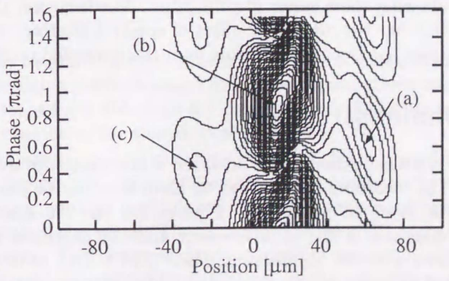

Figure 2.3: The phase-resolved correlation of the signal in Fig. 2.1. We can confirm that the three peaks have different carrier phases.

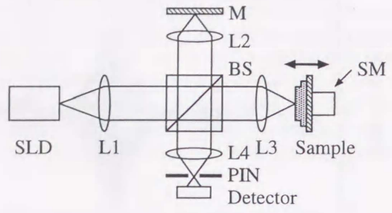

Figure 2.4: The schematic setup of an optical coherence tomography system which is applied to obtain the interferograms. SLD is a super luminescent diode, SM a stepping motor, Ls lenses, M a mirror, BS a beam splitter, PIN a pin-hole, and Detector is an avelantie photo detector. The beam funded out from the SLD is collimated by L1 and splitter to two paths by BS. One of the beam is reflected by M as a reference beam and the other is reflected by a test sample as a probe beam, and then these two beams are interfered on the detector.

600 ms to calculate a phase-resolved correlation. Figure 2.3 shows the result of the phase-resolved correlation. The three peaks (a), (b) and (c) shown in Fig. 2.3 correspond to those in Fig. 2.1. Three peaks appear to be caused by the different beams which are reflected by different depths in the sample because each has a different carrier phase, as shown in Fig. 2.3. To take the opposite example, these peaks would have the same carrier phase if the peaks were reflected at the same point on the sample and subsequently separated by noise or inaccuracy in the measuring system. The resolution of this method is limited by the broader one of the coherence length of the light source or the width of the reference wavelet. The sampling period of the interferogram must be shorter than the half of the carrier wavelength, because of the Nyquist theorem.

As we can see in the example, phase-resolved correlation can separate the peaks in a one-dimensional signal into peaks with a three-dimensional distribution, thus allowing their easier identification. Furthermore, the calculation of the correlation has the additional effect of spectral filtering. Hence, the correlation separates the important signals from the unwanted noise.

2.3 Demonstration

As a more practical example, we analyzed a low coherence interferogram with low SNR. The measured sample was an aluminum mirror coated with an aluminum oxide layer 18 μm thick. Figures 2.4 and 2.5 are respectively the schematic diagrams of the interferometer and the measured sample we used, which includes a super luminescent diode (SLD) light source with a central wavelength of 850 nm and 12 nm spectral width. This interferometer contains a confocal optical setup with lenses L3 and L4, and a pin hall to improve the SNR of interferograms and selectivity of measurement. The SLD beam is split into two optical paths by the beam splitter(BS). One beam is reflected by a plane mirror and acts as the reference beam, and the object beam is reflected and

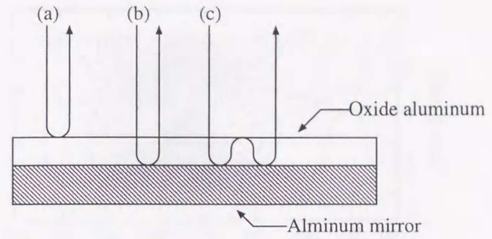

Figure 2.5: The scheme of the measured sample, the an aluminum-oxide coated aluminum mirror. The thickness of the aluminum-oxide layer is 18 mm. The incident beam is reflected in three path; (a) surface reflection, (b) border reflection, and (c) multiple reflection.

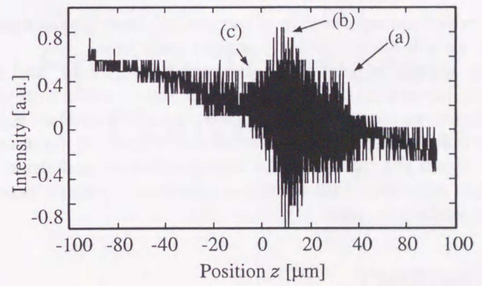

Figure 2.6: Unprocessed low coherence interferogram of the aluminum mirror. Although three signal peaks, (a), (b) and (c) are in fact present, they are masked by noise.

scattered by the measured sample. These two beams are interfered at the photo detector. By scanning the path length difference between these two beams using a stepping motor, we can obtain an low coherence interferogram which contains the depth information of the sample as shown in Fig. 2.6.

This interferogram contains the three peaks which are caused by (a) surface refraction; (b) border refraction between aluminum mirror surface and the aluminum oxide layer; and (c) multiple reflection, but we cannot identify them by means of conventional analysis. This is due to the low SNR and the close proximity of the peaks. The phase-resolved correlation method is able to improve both selectivity and accuracy of identification. In this case, we analyzed the interferogram at only its carrier frequency for the same reason as in the last case, so that the interferogram can be converted to a two-dimensional distribution on a phase(π)-position(z) plane as shown in Fig. 2.7, where positive and negative correlation peak-pairs, such as (b) and (b') can be confirmed. Two peaks in a

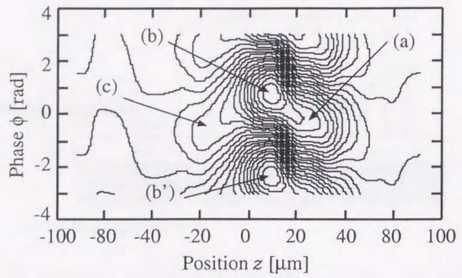

Figure 2.7: The phase-resolved correlation of the signal of Fig. 2.6. The raw signal is spread into a three two-dimensional distribution, ϕ phase, z position.

peak-pair which are separated by π rad. should have the same shape except for their sign, we will discuss only the positive peak here.

We can identify a peak (b) in the center of the plot, and two additional small peaks (a) and (c) to its right and left, all of which have different carrier phases. Hence, we can conclude that there are three separate signals which are caused by different reflections in the sample. Signal (a) represents the surface reflection, signal (b) represents the border reflection and signal (c) represents the multiple reflection. This operation allows us to extract three signal peaks previously masked by noise.

2.4 Summary

We have proposed a new signal analysis method named which we call the 'phase-resolved correlation method'. Most methods which have up to now been applied to interferogram analysis to improve the SNR can separate signals from noise, but are not able to separate independent signals. However, using the phase-resolved correlation method that we propose here, we can clearly identify individual signals. In an experimental demonstration, the method shows its ability to identify a thickness of 18 μm and noise-masked interferogram signal peaks. We have confirmed that this method is very effective for analyzing low coherence interferograms.

Part II

Spatio-Temporal Conversion

As we mentioned in part I, there are some analogies and duality between the temporal and spatial behavior of electric field. The principle of joint trasnform correlator[1] which is one of the most well employed spatial optical computing techniques and a spactral modulating pulse shaper[2, 3] which is one of the most well employed ultrafast pulse controlling techiniques have some analogies. Both of the techiniques modulate the spectrum of an input signal, and the both spectrums are projected spatially. By using the analogy, we can joint these two techniques and the joint system superimposes the auto-correlation of the temporla profile of an input temporal optical signal spatially.

We propose a time-space conversion system, spatio-temporal joint transform correlator in chapter 3. This system projects the auto-correlation of the temporal profile of a femtosecond light pulse spatially. In experimental demonstration, we measure the pulse separations of some picosecond-separated femtosecond twin pulses.

In chapter 4, a spactral interferometric optical coherence tomography system is investigated as a more practical application of spatio-temporal joint transform optical coherence tomography system. This system is an all-optical, less spatial scanning optical coherence tomography system, which determines the three dimensional profile of a test object with an one-dimensional mechanical scanning operation.

Chapter 3

Spatio-Temporal Joint Transform Correlatior

3.1 Introduction

In recent years, large numbers of demonstrations and applications in the field of optical computing based on the high parallelism, high processing speed and high capacity of light have been studied. These techniques can be classified into two broad categories. One is spatially discrete optical computing represented by an optical neural network technique or the like[16, 17]. Although these techniques are based on the parallelism of light, diffraction and interference, the fundamental properties of light are not availed. The other is a group of techniques which are based on optical Fourier transform of Fraunhofer diffraction[1]. In these techniques, which are represented by a joint transform correlator (JTC)[18] or optical matched filtering[1], the two-dimensional spatial spectrum of an image is spread spatially by the Fourier transform ability of a lens and is modulated, and so the original image is manipulated indirectly.

Meanwhile due to the progress of solid state lasers and mode-locking techniques, some pulse laser sources with very short temporal duration have been available that do not demand high costs or difficult operation. In accordance with the uncertainty of Fourier transform, such pulses have very broad wavelength spectra, in contrast to their very short temporal duration. Therefore spectral filtering methods have been used to control the temporal profiles of such short pulses[5, 19, 6, 20]. In the methods, the broad wavelength spectrum of the pulse is spread spatially by a grating-lens pair and modulated by some kind of modulating devices, for instance a liquid crystal spatial light modulator (LC-SLM), an acousto-optic (AO) crystal, a photorefractive crystal or the like. Then the modulated spectrum is converted to a temporal pulse by another grating-lens pair. As a result the temporal profile of the light pulse can be controlled arbitrarily but indirectly, although its temporal duration is too short to be controlled directly.

In the above discussion, we can find much similarity between the two techniques, an optical computing technique and a spectral filtering method. The similarity is that both of the input signals, a two-dimensional optical image in the optical computing method and a temporal pulse in the spectral filtering

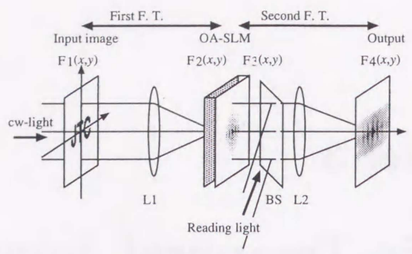

Figure 3.1: The schematic setup of conventional JTC. L1, L2 are nlens, F.T Fourier transform, and OA-SLM optically addressed spatial light modulator. The auto-correration of an input image is observed on an output plane.

method, are Fourier transformed by a Fourier transform lens or a grating-lens pair, and the spatial or wavelength spectrum is spread spatially. Then the spectrum is modulated and transformed again to the original domain.

By using the similarity, we can achieve time-space conversion. In the above methods, both the temporal spectrum and the spatial spectrum are spread spatially. Hence we can connect these two methods at the spectral plane. For instance, Nuss *et al.*[21] demonstrated that when the spatially spread power spectrum of an input pulse was recorded on a photo-refractive device spatially, then the spatial pattern was able to be read out and Fourier transformed by a lens and cw-laser. As a result, the temporal profile of the pulse was projected spatially. For another example, Ema *et al.*[22] demonstrated another method. In this method, the phase term of the spatially spread spectrum of an input pulse which rapidly changes temporally is canceled out by a reference beam on a non-linear crystal. Hence, we can get the temporal profile of an input pulse spatially by a grating-lens pair and a Fourier transform lens.

In this paper, by using the similarity more directlly, we propose and demonstrate a spatio-temporal joint transform correlator (ST-JTC)[23] which spatially projects the cross-correlation of pulses which propagate on the same longitudinal axis. In this system, the wavelength spectrum is spatially distributed by a grating-lens pair, which is the technique of a spectral filtering method. Then the distributed spectrum is converted to a spatially one-dimensionally distributed power spectrum by an optically addressed spatial light modulator (OA-SLM) and spatially Fourier transformed by a lens and cw-laser, which is the technique of a conventional spatial JTC. As a result, we can obtain the temporal auto-correlation of the input pulse spatially on an output plane. To sum up the system, it is a conventional JTC except that the first spatial Fourier transform is replaced with temporal Fourier transform by a grating-lens pair. Therefore, it is a JTC which accepts a temporal signal as an input and puts out a spatial signal as an output.

3.2 Principle

First, we would describe a conventional spatial JTC which has already been widely investigated. A typical setup of a JTC system is shown in Fig. 3.1. We assume that the field amplitude of a two-dimensional image on the input plane in Fig. 3.1 is expressed as $F_1(x,y)$, and consider the process of obtaining its auto-correlation by a JTC. In the first step, the image $F_1(x,y)$ is decomposed to its spatial spectrum by cw-laser and a Fourier transform lens. The field amplitude on the focal plane of the lens L_1 becomes

$$F_2(x,y) = \frac{\exp\left(i\frac{\pi}{2}\right)\exp\left(-i2kf_a\right)}{\lambda f_a}\hat{F}_1\left(\frac{x}{\lambda f_a},\frac{y}{\lambda f_a}\right) \tag{3.1}$$

where $\hat{F}_1(\mu,\nu)$ is the Fourier transform of $F_1(x,y)$ which is defined as

$$\hat{F}_1(\mu,\nu) = \iint_{-\infty}^{\infty} F_1(x,y)\exp\left\{i2\pi\left(x\mu+y\nu\right)\right\}dx\,dy, \tag{3.2}$$

λ and k are the wavelength and the wave number of the laser, f_a the focal length of the lens, L_1 and μ, ν spatial frequency. In the next step, the spectrum is converted to its intensity, the power spectrum of $F_1(x,y)$ by an OA-SLM or a CCD camera and an SLM.

$$F_3(x,y) = \left|\hat{F}_2\left(x,y\right)\right|^2 \propto \left|\hat{F}_1\left(\frac{x}{\lambda f_a},\frac{y}{\lambda f_a}\right)\right|^2 = \hat{F}_1\left(\frac{x}{\lambda f_a},\frac{y}{\lambda f_a}\right)\times\hat{F}_1{}^*\left(\frac{x}{\lambda f_a},\frac{y}{\lambda f_a}\right) \tag{3.3}$$

Here $\hat{F}_1{}^*$ means the complex conjugate of $\hat{F}_1$. Finally, the power spectrum is Fourier transformed again by another lens. As a result, the field amplitude on an output plane is expressed as

$$\begin{aligned} F_4(x,y) &= \frac{\exp\left(i\frac{\pi}{2}\right)\exp\left(-i2kf_a\right)}{\lambda f_a}\hat{F}_3\left(\frac{x}{\lambda f_a},\frac{y}{\lambda f_a}\right) \\ &\propto -\iint_{-\infty}^{\infty} F_1\left(-\frac{f_a}{f_b}x',-\frac{f_a}{f_b}y'\right)F_1\left(-\frac{f_a}{f_b}x'-\frac{f_a}{f_b}x,-\frac{f_a}{f_b}y'-\frac{f_a}{f_b}y\right)dx'\,dy' \\ &= F_1\left(-\frac{f_a}{f_b}x,-\frac{f_a}{f_b}y\right)\otimes F_1\left(-\frac{f_a}{f_b}x,-\frac{f_a}{f_b}y\right) \end{aligned} \tag{3.4}$$

where f_b is the focal length of the lens L_2, and $\otimes$ correlation operator. Note that the phase term has dropped out, because we detect only the intensity of F_4. From this equation, we can confirm that the output, F_4 becomes the auto-correlation of $F_1\left(-f_a/f_b x,-f_a/f_b y\right)$.

Next, we explain our novel optical system, ST-JTC, which is the subject of this chapter. The schematic setup of the system is shown in Fig. 3.2. The system is a conventional JTC except that the lens for spatial Fourier transform is replaced by a grating-lens pair for temporal Fourier transform. The temporal and spatial Fourier transform in Fig. 3.2 correspond to first and second Fourier transform in Fig. 3.1, respectively. When the profile of an input pulse just before the grating is given by $E_1(x,t) = S(x)T(t)$, where $S(x)$, $T(t)$ are the spatial

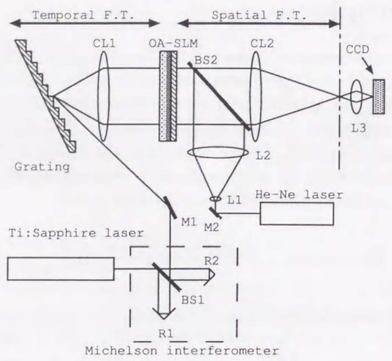

Figure 3.2: The schematic setup of a spatio-temporal JTC. CL cylindrical lens, BS beam splitter, OA-SLM optically addressed spatial light modulator, He-Ne laser is 632.8-nm wavelength cw-lasercw-laser and Ti:Sapphire Laser is 800.0-nm wavelength and 120-fs FWHM mode-locked pulse laser, and F. T. means Fourier Transform. The temporal power spectrum of input pulses are spread on the left side of the OA-SLM spatially, then the spectrum are read out by cw He-Ne laser then Fourier transformed by CL2. Therefore, the temporal correlation of the input pulses are appeared on the CCD spatially.

and temporal profiles of the pulse respectively and x and t are transverse spatial axis and temporal axis, the field amplitude after the grating is given by

$$E_2(x, z=0, t) = S(\alpha x) T(t - \beta x) \exp\left(i2\pi \frac{c}{\lambda_w} t\right) \tag{3.5}$$

where $\alpha = \cos\theta_i / \cos\theta_d$, $\beta = \lambda_w N / \cos\theta_d$. θ_i and θ_d are the incident angle and diffraction angle of the grating, N the grating constant, λ_w the central wavelength of the input pulse and c the velocity of light. Then E_2 is Fourier transformed by a lens and spread on the left side, the writing side, of an OA-SLM as

$$E_3 \propto \hat{S}\left(\frac{\alpha}{\lambda_w f_w} x\right) * \hat{T}\left(-\frac{\alpha}{\beta \lambda_w f_w} x\right) \simeq \hat{T}\left(-\frac{\alpha}{\beta \lambda_w f_w} x\right) \tag{3.6}$$

where f_w is the focal length of CL_1[24]. The approximation is made when the spatial extent of the pulse is much larger than its temporal duration, and the phase terms are ignored to simplify the expression. From this equation, we can confirm that the temporal Fourier transform of the pulse is spread spatially on the plane. Then the field amplitude is converted to its intensity, the power spectrum, by the OA-SLM.

$$E_4 = \hat{T}\left(-\frac{\alpha}{\beta \lambda_w f_w} x\right) * \hat{T}^*\left(-\frac{\alpha}{\beta \lambda_w f_w} x\right) \tag{3.7}$$

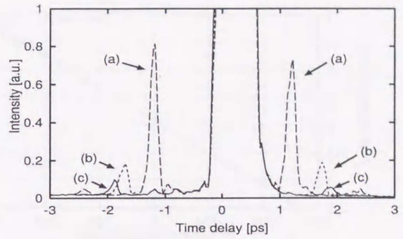

Figure 3.3: The auto-correlations of twin pulses with 1.02-ps (a), 1.38-ps (b) and 1.53-ps (c) separations, which are measured by the spatio-temporal JTC. We can confirm that the correlation peaks are shifting with the separation of the input pulses.

Finally, the power spectrum is read out with λ_r wavelength cw-laser and spatially Fourier transformed by a f_r focal length lens, CL_2. Hence the field amplitude on the output plane is expressed as

$$E_5 \propto T\left(-\frac{\beta \lambda_w f_w}{\alpha \lambda_r f_r} x\right) \otimes T\left(-\frac{\beta \lambda_w f_w}{\alpha \lambda_r f_r} x\right). \tag{3.8}$$

This equation states that the temporal auto-correlation of the input pulse is spread spatially on the output plane.

3.3 Experimental Demonstration

We have demonstrated the ST-JTC. In the demonstration, we use twin pulses which are synthesized by a Michelson interferometer as an input pulse signal. A parallel-aligned nematic liquid crystal spatial light modulator (PAL-SLM) manufactured by HAMAMATSU[25] is used as an OA-SLM, and the output-correlation image is detected by a CCD camera. The schematic setup has been in Fig. 3.2; the focal length of CL1 and CL2 is 130 mm and 200 mm, respectively, the grating constant of the grating is 2000 lp/mm and the cw-laser source is a He-Ne laser with 632.8-nm wavelength. We placed an objective lens in front of the CCD camera to magnify the correlation image. Auto-correlations of the twin pulses which were observed in the experiment are shown in Fig. 3.3. The pulse separation of the input twin pulses are 1.02 ps, 1.38 ps and 1.53 ps. Their auto correlations are respectively shown in peaks (a), (b) and (c). Hence we can confirm that the separation between the $\pm$1st order peaks of the correlations are in proportion to the separations of the pulses. In the figure, although the longitudinal axis is calibrated to a temporal scale, it originally means the spatial scale on the CCD camera.

On the other hand, in Fig. 3.4, the separations between $\pm$1st correlation peaks on the CCD camera are plotted against the displacement of an arm of the Michelson interferometer which corresponds to the separations of input twin pulses. According to the plot, the root-mean-squared error of the ST-JTC is

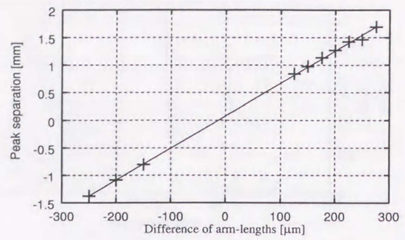

Figure 3.4: ±1st order peak separation on the CCD versus the displacement of the arm of the Michelson interferometer. The displacement is in proportion to the separation of separations of the input twin pulses.

determined as 29.8 μm on the CCD camera, or 12.4 fs in the temporal domain.

3.4 Summary

We have proposed and demonstrated a novel optical system, a spatio-temporal joint transform correlator (ST-JTC). The system based on similarity between a conventional spatial joint transform correlator, which is one of the most popular optical computing technique and a spectral filtering method, which is one of the most popular method of controling the temporal profile of an ultrafast light pulse. Our system is a hybrid of these two methods. In the demonstration, we determined the pulse separations of twin pulses which were synthesized by a Michelson interferometer. According to the result, we have confirmed that the experimental system has 12.4 fs temporal accuracy in determining the positions of input pulses.

As eq. 3.8 describes, the correlation which derived here is not an intensity one but a complex correlation which includes information on the phase of the pulse. The ST-JTC does not depend on nonlinearity which depends on the high peak intensity of a pulse. This means that, we can use a super luminescent diode (SLD) or any other broad band light source as the input light source. With such light sources, the spatial output becomes the temporal coherence function of the input light source. Although in the demonstration presented in this paper the input signal was generated by a Michelson interferometer, if the signal is generated by surface reflection or the like, the system could work as a white light interferometer without scanning operation. Based on the idea, we are now constructing a non-scanning and all-optical optical coherence tomography system to measure the *in vivo* structure of human skin[26].

As mentioned in the introduction, the ST-JTC is based on the idea of a spatial JTC. So, almost all techniques of conventional JTC can be applied to the ST-JTC, such as nonlinear thresholding to increase the S/N ratio[27] or signal retrieval from rough phase noise[28]. Such unification of pulse control and conventional optical computing should yeild a breakthrough in optical computing. Computational long distance communication and computational measurement

should thus become possible.

Chapter 4

Spectral Interferometric Joint Transform Optical Coherence Tomography

4.1 Introduction

Optical coherence tomography (OCT) or a white light interferometer is one of the most commonly adopted methods for three-dimensional profile measurement and uses a broad-band, low coherence light source. The object to be measured is placed on the end of one arm of the Michelson interferometer. The scattered light from the object and a reference beam which passes through the other arm make an interference fringe on a photodetector. The interferogram can be used to analyze the depth information of the sample object to an accuracy determined by the temporal coherence length of the light source[29, 30, 31].

Use of a confocal optical setup or an optical fiber interferometer makes the OCT system most suited to measuring light-scattering objects. This system is widely used in the biomedical field in *in vivo* measurements[13, 32, 14]. However, the use of a confocal setup sacrifices one advantage of optical measurement, namely the spatial parallelism of light. Without this advantage, to determine an object three-dimensionally, the system requires a three-dimensional scanning process which includes one-dimensional arm-length scanning using the Michelson interferometer to determine depth information at one point on the measured object, and additional two-dimensional perpendicular scanning operations to determine the depth information two-dimensionally. This type of mechanical scanning operation is very time-consuming, making it impractical for measuring the structure of *in vivo* objects.

To remove the one-dimensional depth scanning and to avoid this long measurement time, a spectral interferometer technique has been introduced to some OCT systems[33, 34]. Usually, this type of OCT setup includes a Michelson interferometer as part of the conventional OCT setup. In systems such as this, the temporally encoded depth information is not decoded by scanning the path-length of the Michelson interferometer as would be done using an ordinary OCT system. Instead, it is decoded by a spectrometer. The output light of a Michel-

son interferometer is temporally Fourier transformed by means of a grating-lens pair. Since the spatially spread spectrum includes the depth information, the depth structure of the object can be derived by Fourier transforming the spectrogram. This process does not demand mechanical scanning, and therefore, the three-dimensional scanning operation is reduced to a two-dimensional version.

We have presented a spatio-temporal joint transform correlator (ST-JTC)[35], which is based on the principle of femtosecond pulse shaping by spectral modulation[2, 3, 36, 37] and a joint transform correlator, one of the most commonly used spatially optical computing techniques[1]. In the spatio- temporal JTC, the temporal information of an ultrafast light pulse or a pulse train is spatially spread into its spectrum by a grating-lens pair. The spectrum is then spatially Fourier transformed by an optically addressed spatial light modulator (OA-SLM) and a cylindrical lens. This makes it possible to obtain the temporal correlation of the input pulse as a spatial image. In this case, the correlation is not an intensity correlation but a phase correlation. Hence, when continuous wave (cw) broadband light is incident to the system, we are able to obtain its coherence function on the output plane. The spatio-temporal JTC may also be regarded as an all-optical spectral interferometer. Furthermore, the system can be spatially one-dimensionally multiplexed due to the spatial parallelism of light. So the scanning dimension in OCT can be reduced to one dimension if the spatio-temporal JTC technique is introduced to the spectral interferometric OCT system.

In this chapter, we apply the spectral interferometry to an OCT system to avoid the depth directed scanning operation, and also apply the spatio-temporal JTC technique to reduce one more scanning dimension and to carry out optical Fourier transform. This system does not demand electronic computation to obtain the object image, and so it can be implemented as an all-optical setup, thus allowing the measurement time to be dramatically shortened.

4.2 Principle of Spectral Interferometric OCT

An OCT system which uses a white light interferometer encodes the depth information of a measured object in the temporal complex amplitude profile of the reflected beam. When few micrometer depth information is encoded to the reflected beam, the temporal profile changes very rapidly because a depth of 1 μm is encoded in 6.6 fs, furthermore when we use a cw broadband light source, the depth information is encoded in the phase of the light, not intensity. This means that the depth profile of an object is not measured directly even if a photo detector has enough high response speed. In an ordinary OCT system, to detect the fast signal by a slow detector and measure the invisible phase changing, the reference beam and the object beam are interfered by the Michelson interferometer to obtain the correlation signal which contains the depth information of the object. One-dimensional scanning operation of one arm of the Michelson interferometer is required to obtain depth information on the object.

To avoid the need for mechanical scanning, we applied the principle of spectral interference and a joint transform correlator to an OCT system. The schematic setup of the system of the non-scanning spectral interferometer is shown in Fig. 4.1. The optical system is in three parts. The first part is a signal generator, which uses light nto encode the three-dimensional shape of

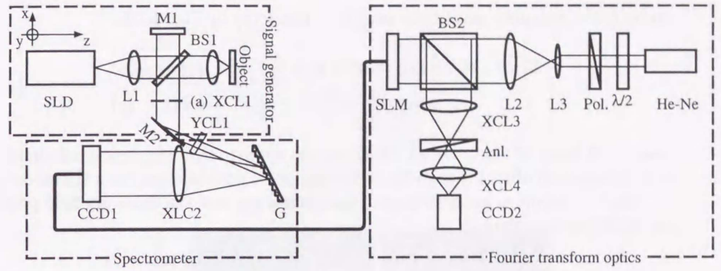

Figure 4.1: Schematic setup of the spectral interferometric joint transform OCT system. SLD super luminescent diode, L lens, XCL and YCL x and y oriented cylindrical lenses, BS beam splitter, M mirror, G grating, $\lambda/2$ half-wavelength plate, pol. polarizer and anl. analyzer.

the sample object. We used the Michelson interferometer with its arm-length shifted several hundred micrometers from its zero point. In a spectrometer, the temporally encoded depth information is spread along the spatial axis as a spectral interferogram. The last part of the Fourier transform, the spatially spread spectral interferogram is Fourier transformed spatially. As a result, the sectional image of the surface under test is obtained by CCD2.

First, we assume the spectral profile of the broadband light source to be

$$\hat{E}_0^t(\nu) = \exp\left\{-\pi\left(\frac{\nu}{\gamma}\right)^2\right\}\exp\{i\phi(\nu)\} \tag{4.1}$$

where ν is temporal frequency and γ is a constant which is determined by the temporally spectral width. The first term of $\exp\left\{-\pi\left(\nu/\gamma\right)^2\right\}$ represents the Gaussian spectral intensity profile, and the second term $\exp\{i\phi(\nu)\}$ is the phase of the spectrum. In the experiments, we use a super luminescent diode (SLD) as the light source, and so $\phi(\nu)$ should be a random function of ν. The central wave length and FWHM of the spectrum are 851 nm and 12 nm, respectively. Hence, $\gamma = 5.37 \times 10^{12}$. The inverse-Fourier transform of the electric field, the temporal profile of the light source is expressed as

$$E_0^t(t) = \gamma\exp\left\{-\pi\left(\gamma t\right)^2\right\} * \Phi(t) \tag{4.2}$$

where $\Phi(t)$ is the inverse-Fourier transform of $\exp\{i\phi(\nu)\}$ and $*$ denotes convolution. $\Phi(t)$ has a temporally constant intensity profile which is based on the randomness of $\phi(\nu)$. Hence $E_0^t(t)$ also has a temporally constant intensity profile.

Let us consider the electric field after the signal generator, the first part of the optical system. Assuming the difference of the arm-length of the interferometer

to be l, the complex amplitude profile of point (a) in Fig. 4.1 is

$$\begin{aligned} E_1^t(t) &= \gamma \exp\left[-\pi\left\{\gamma\left(t+\tfrac{l}{2c}\right)\right\}^2\right] * \Phi(t+\tfrac{l}{2c}) \\ &\quad +\gamma \exp\left[-\pi\left\{\gamma\left(t-\tfrac{l}{2c}\right)\right\}^2\right] * \Phi(t-\tfrac{l}{2c}) \end{aligned} \tag{4.3}$$

where c is speed of light. By eq. (4.3), we can confirm that the depth information of the measured object is encoded in the temporal optical signal as a signal-delay.

After the spectrometer section of the optical system, the intensity field profile on CCD1 is described as

$$\begin{aligned} \left|\hat{E}_2^s(x)\right|^2 &\propto \exp\left\{-2\pi\left(\tfrac{\nu_1\alpha}{cf_1\beta}\gamma x\right)^2\right\} \\ &\quad \left\{1+\cos\left(2\pi\tfrac{\nu_1 l\alpha}{c^2 f_1\beta}x\right)\right\} \end{aligned} \tag{4.4}$$

where ν_1 is the central frequency of the SLD, f_1 is the focal length of XCL2 and α and β are constants determined by the grating, G as $\alpha = \cos\theta_i/\theta_d$ and $\beta = N/(\nu_1 \cos\theta_d)$. The electric field have temporally constant intensity profile, so that the expression is temporally integrated. The angles θ_i and θ_d are the incident and diffraction angle of the grating and N is the grating constant[24, 38, 39, 40]. The first term of eq. (4.4) expresses the spectral intensity profile of the SLD, the light source. The second term forms a sinusoidal wave with its frequency in proportion to the path length difference of the interferometer.

The intensity profile detected by CCD1 is written on a spatial light modulator (SLM) and read out by a cw-He-Ne laser and spatially one-dimensionally Fourier transformed by a cylindrical lens, XCL3. As a result, an $E_3^s(x)$ is obtained on CCD2.

$$\begin{aligned} E_3^s(x) &\propto \exp\left\{-2\pi\left(\tfrac{\nu_2 f_1\beta}{\nu_1 f_2\alpha}\gamma x\right)^2\right\} \\ &\quad * \left\{\tfrac{1}{2}\delta\left(\tfrac{\nu_2}{cf_2}x - \tfrac{\nu_1\nu_2\alpha}{2c^3 f_1 f_2\beta\gamma}l\right) + \delta\left(\tfrac{\nu_2}{cf_2}x\right)\right. \\ &\quad \left. +\tfrac{1}{2}\delta\left(\tfrac{\nu_2}{cf_2}x + +\tfrac{\nu_1\nu_2\alpha}{2c^3 f_1 f_2\beta\gamma}l\right)\right\} \end{aligned} \tag{4.5}$$

where ν_2 is the central frequency of the He-Ne laser. Using eq. (4.5), we can confirm that the positions of the delta functions on CCD2 represent the path length difference of the interferometer. The position of the delta functions represent the depth of the sample object, enabling the depth structure of the object to be determined by this system.

4.3 Experiments

We have measured the path length difference of the Michelson interferometer and three-dimensional profiles of two objects by a spectral interferometric joint transform OCT system, shown in Fig 4.1. In the experiment, an SLD with a central wavelength 850 nm and 12 nm FWHM of spectrum is used as a cw broad band light source and a PAL-SLM[41, 42, 43], parallel aligned nematic liquid crystal SLM is used as the SLM.

First, to calibrate the system, we measured the path length difference of a the Michelson interferometer. In this case, plane mirrors are placed on the ends

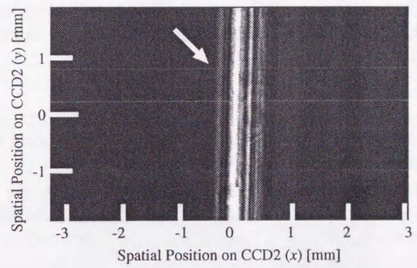

(a)

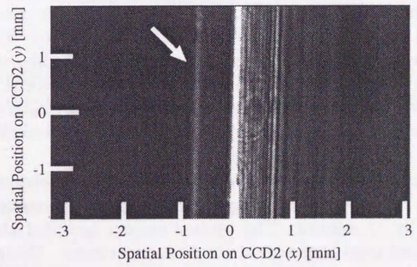

(b)

Figure 4.2: Output image of the OCT system. Correlation peaks which correspond to the path length difference of the two arms of a Michelson-interferometer.

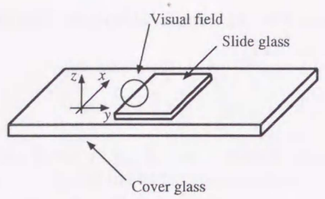

Figure 4.3: Schematic figure of the sample object used in the second experiment. Nail varnish has been used to adhere together the glass sheets, and the surface is coated with aluminum.

of the two arms of the interferometer. The two cylindrical lenses, XCL1 and YCL1 which are shown in Fig. 4.1 are removed.

The results are shown in Fig. 4.2. In Fig. 4.2-(a), we can see an auto-correlation peak of an input signal (0th order peak), halation noise and 1st order cross correlation peak on the left side of the 0th order peak, indicated by the white arrow. The position of the 1st order peak represents the path length difference. In the case of Fig. 4.2-(b), one arm-length is 400 μm longer than in the case of (a). Hence, the 1st order peak shifts in proportion to the arm-length shift. From these results, we calculated the coefficient between the arm-length difference and the spatial position on CCD2 as 16 μm/pixel. Thus the coefficient gives the measurement accuracy of this system. According the FWHM of the auto-correlation peaks, the depth resolution of the system is determined as 70 μm. And, according to the numerical apertures of cylindrical lenses and the central wavelength of the SLD light source, the x-resolution and y-resolution are estimated as 2 μm and 4μm, respectively.

In the next experiment, we measured the sample object with a stepped surface shown in Fig. 4.3. The sample is constructed of a cover glass and a glass slide covered by aluminum. The optical system included the two cylindrical lenses which had been removed in the first experiment. Using XCL1, the light is focused on the measured sample, improving the resolution in the x-direction. Furthermore, XCL1 corrects the direction of the reflected light, presumably leading to reduced light power loss. The image of the object surface is formated on CCD1 by the YCL1, resulting in improved resolution in the y-direction. In this system, the scanning operation along the z-axis runs in parallel with spectral interferometry. Hence, we have to carry out only one-dimensional scanning in the x-direction to measure the three-dimensional profile of the object In this experiment, we scanned 50 points and reconstructed the object surface as shown in Fig. 4.4. The stepped surface of the object can be observed.

In the next experiment, we measured the surface of the Japanese ten-yen-coin shown in Fig. 4.5. The coin is made from copper with a rough surface and the probe light is scattered by the surface. The measured and reconstructed surface image is shown in Fig. 4.6. The measured area is cropped into a rectangle in Fig. 4.5. Figure 4.6 shows the reconstructed surface shape as a topographic image in which bright points indicate higher points and dark points indicate lower points. This example indicates that we can confirm that this system has

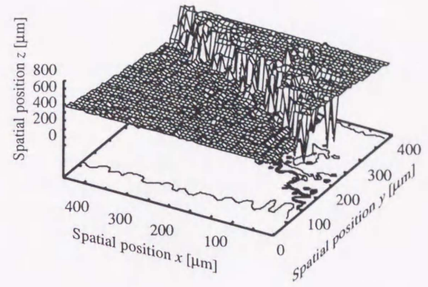

Figure 4.4: The Measured three-dimensional surface of the sample shown in Fig. 4.3.

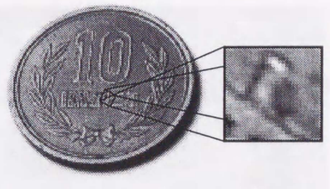

Figure 4.5: Photograph of the sample object used in the third experiment, a Japanese 10 yen coin. The area which is cropped to a rectangle is measured using the system.

the ability to measure the shape of an rough surface.

4.4 Summary

We have constructed a spectral interferometric three-dimensional surface-measurement system with only one-dimensional scanning operation and without the need for electronic computation.

In this chapter, we measured three samples to a depth-accuracy of 16 μm and depth-resolution of 70 μm. One is the path length difference of the Michelson interferometer, another is the surface of an aluminum coated sample and the last is the rough surface of a coin. Although the last sample is a highly light-scattering object, the system has demonstrated its ability to measure minute changes in the height of a sample surface.

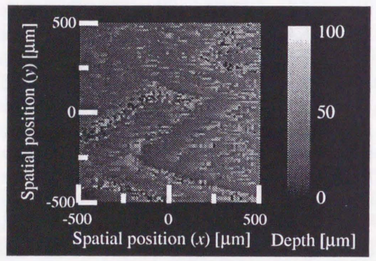

Figure 4.6: The measured surface image of a 10 yen coin. Although the signal-to-noise ratio is not ideal, we can identify a part of the Japanese character "+" (ten).

Part III

Spatio-Temporal Coupling

In some diffractive optical systems, such as a spectrometer or a pulse shaper, spatio-temporal coupling is induced. By the coupling effect, the spatial state of an electric field is determined by not only its ex-spatial state, but also its ex-tempral state. As the same, the temporal state of the electric field is determined by its ex- temporal and spatial profile.

In the most cases, such coupling effect causes the decreasing of accuracy of spectroscopy or pulse control. Such non-demanded phenomena are not avoidable but easily redusable, so that in many case the effects are ignored.

We can, however, activelly apply the effect to achive more higher order spatio-temporal computing. Employing the effect, for example, we can control the spatial and temporla profile of a femtosecond light pulse by a one-dimensional spatial light modulator.

In this part, we investigate the applications of spatio-temporal coupling. The spatio-temporal Wigner distribution function is introduced to analyze the spatio-temporal properties of an optical system with less amount of numerical calculation. In chapter 5, we analyze the spatio-temporal coupling effect of conventional pulse shaper. In chapter 6, an improved pulse shaper, spatio-temporally coupled pulse shaper is introduced, and analyzed numerically. The pulse shaper controls the spatial and temporal profile of a femtosecond light pulse at the same time. In chapter 7, the spatio-temporal properties of a time-domain microscope is numerically analyzed.

Chapter 5

Spatio-Temporal Coupling in Pulse Shaper

5.1 Introduction

Improvements in laser techniques have made it easier to apply high precision femtosecond lasers to many fields, including communications, medical equipment, optical measurements and industrial fabrication [44, 4, 45, 46]. Such applications demand detectors or modulators which work at femtosecond speeds, but such devices have yet to be created. Instead, pulse-shapers are widely applied to control ultrafast light pulses. A pulse-shaper spatially spreads the spectral components of an ultrafast light pulse using a grating-lens pair, modulates the spectrum by means of a spatial light modulator (SLM) or the like, then reconstructs the temporal pulse from the modulated spectrum by means of another grating-lens pair. Using a pulse-shaper makes it possible to control the temporal profile of an ultrafast light pulse without the need for high speed devices.

In a pulse-shaper or a spectrometer, spatio-temporal coupling effect [47][48] are unavoidable. As a result of diffraction, the temporal profile of an electric field is influenced by its previous spatial profile, and the spatial profile of an electric field is influenced its previous temporal profile. In some applications, the spatio-temporal coupling creates problems, such as spatial and/or temporal defocus or spatial and/or temporal chirp, but it is possible to reduce this effect by simple means. For example, in a pulse-shaper or a spectrometer, we can ignore the coupling if the spatial beam shape is sufficiently wider than its temporal version[49]. On the other hand, it is also possible to apply actively the spatio-temporal coupling by understanding the behavior of the coupling both intuitively and quantitatively.

Payne *et al.* analyzed the property of a pulse-shaper using the Wigner distribution function. Although, in his paper, he analyzed an ideal pulse-shaper, without any misalignment or defocus, it is likely that spatio-temporal coupling will occur in a non-ideal pulse-shaper.

In this paper, we analyze the spatio-temporal properties of a pulse-shaper in which we take into account defocus of lenses, grating pairs with different grating constants, lenses with different focal lengths and combinations of these factors

by using the Wigner distribution function.

5.2 Principle of the Wigner Distribution Function

The Wigner distribution function was originally introduced to quantum dynamics to represent position-momentum intensity distribution containing uncertainty due to having been Fourier transformed[50]. By introducing this function to light waves, we can obtain the space-to-spatial frequency or time-to-temporal frequency distribution of photons, although the physical quantities have uncertainty with respect to each other due to Fourier transform. The Wigner expression of spatial and temporal electric field amplitude $E(x,t)$ is defined as

$$W^{ST}(x,\xi,t,\omega) = \frac{1}{2\pi}\iint_{-\infty}^{\infty} E\left(x+\frac{x'}{2},t+\frac{t'}{2}\right)E^*\left(x-\frac{x'}{2},t-\frac{t'}{2}\right) \times \exp\{i(-\xi x'+\omega t')\}\,dx'dt' \quad (5.1)$$

where x is the spatial position, ξ is the spatial frequency, t is the time and ω is the temporal frequency. This distribution function represents the intensity distribution of complex light amplitude in four-dimensional (x,ξ,t,ω) space, so that we can arbitrarily obtain the one to four-dimensional distribution by integrating Eq. (5.1) along x, ξ, t and/or ω. By representing the input and output field intensity of a linear optical setup using the Wigner function, the property of the optical setup is expressed as a linear coordinate transformation[51]. When a phase modulating optical element, such as a lens, phase-modulator, dispersion medium or spatial diffraction is described as a four-dimensional function, $\Phi(x,\xi,t,\omega)$, its partial differentiation $\partial\Phi/\partial x$, $\partial\Phi/\partial\xi$, $\partial\Phi/\partial t$ and $\partial\Phi/\partial\omega$ reveals the group velocity delay of ξ, x, ω and t, respectively. Hence, the output four-dimensional coordinate is expressed by subtracting the group delay from the input coordinate. For example the coorndinate transform matries represent a lens, Fresnel diffraction and diffraction grating are

$$\begin{bmatrix} x_o \\ \xi_o \\ t_o \\ \omega_o \end{bmatrix} = \begin{bmatrix} 1 & 0 & 0 & 0 \\ k_0/f & 1 & 0 & 0 \\ 0 & 0 & 1 & 0 \\ 0 & 0 & 0 & 1 \end{bmatrix} \begin{bmatrix} x_i \\ \xi_i \\ t_i \\ \omega_i \end{bmatrix}, \quad (5.2)$$

$$\begin{bmatrix} x_o \\ \xi_o \\ t_o \\ \omega_o \end{bmatrix} = \begin{bmatrix} 1 & -z/k_0 & 0 & 0 \\ 0 & 1 & 0 & 0 \\ 0 & 0 & 1 & 0 \\ 0 & 0 & 0 & 1 \end{bmatrix} \begin{bmatrix} x_i \\ \xi_i \\ t_i \\ \omega_i \end{bmatrix}, \quad (5.3)$$

and

$$\begin{bmatrix} x_o \\ \xi_o \\ t_o \\ \omega_o \end{bmatrix} = \begin{bmatrix} \alpha & 0 & 0 & 0 \\ 0 & 1/\alpha & 0 & -\beta/\alpha \\ -\beta & 0 & 1 & 0 \\ 0 & 0 & 0 & 1 \end{bmatrix} \begin{bmatrix} x_i \\ \xi_i \\ t_i \\ \omega_i \end{bmatrix}. \quad (5.4)$$

The conversion rule allows us to intuitively understand the behavior of the optical setup.

The coordinate transform of a complex optical setup is calculated as a cross-product of the transform matrixes of its elements. For example, a transform matrix of a 2-f spatial Fourier transform setup, which is constructed from f-Fresnel diffraction, a lens whose focal length is f and another f-Fresnel diffraction is expressed as

$$\begin{bmatrix} x_o \\ \xi_o \\ t_o \\ \omega_o \end{bmatrix} = \begin{bmatrix} 0 & -\frac{f}{k_0} & 0 & 0 \\ \frac{k_0}{f} & 0 & 0 & 0 \\ 0 & 0 & 1 & 0 \\ 0 & 0 & 0 & 1 \end{bmatrix} \begin{bmatrix} x_i \\ \xi_i \\ t_i \\ \omega_i \end{bmatrix} \quad (5.5)$$

where (x_i,ξ_i,t_i,ω_i) and (x_o,ξ_o,t_o,ω_o) are the input and output coordinates, k_0 is the transverse wave number which is determined as $2\pi/\lambda_0$ and λ_0 is the wavelength of the light.

The 3-3, 3-4, 4-3 and 4-4 elements of Eq. (5.5), the temporal partial matrix form a unit matrix, so that it does not change the temporal profile of the electric field. On the other hand, according to the 1-1, 1-2, 2-1 and 2-2 elements of Eq. (5.5), the spatial partial matrix, the spatial and spatial-frequency profile of the electric field are swapped. This means that the optical setup can be Fourier transformed, spatially.

The transform matrix of a spectrometer, which is constructed from a 2-f Fourier transform setup and a diffraction grating, is expressed as

$$\begin{bmatrix} x_o \\ \xi_o \\ t_o \\ \omega_o \end{bmatrix} = \begin{bmatrix} 0 & -\frac{\alpha f}{k_0} & 0 & 0 \\ \frac{k_0}{\alpha f} & 0 & 0 & -\frac{\beta}{\alpha} \\ 0 & \frac{\beta f}{k_0} & 1 & 0 \\ 0 & 0 & 0 & 1 \end{bmatrix} \begin{bmatrix} x_i \\ \xi_i \\ t_i \\ \omega_i \end{bmatrix} \quad (5.6)$$

where $\alpha = \cos\theta_i/\cos\theta_d$, $\beta = 2\pi p/(\omega_0 d\cos\theta_d)$, θ_i and θ_d are the incident and diffraction angle to the grating, respectively, p is the diffraction order and ω_0 is the central frequency of the light. We can confirm the ξ-ω and t-ξ coupling in the spectrometer by means of Eq. (5.6).

5.3 Analysis of the Spatio-Temporal Properties of Pulse-Shapers

In this section, we numerically analyze the spatio-temporal properties of several pulse-shapers. The first model is an ideal pulse-shaper, and others are misaligned, have input and output gratings with different grating constants, have lenses with different focal lengths, and have different grating constants and focal lengths.

5.3.1 An Ideal Pulse-Shaper

We numerically analyzed the spatio-temporal property of a pulse-shaper schematically illustrated in Fig. 5.1. In this system, we ignore the dispersion caused by

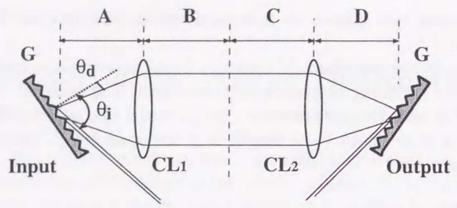

Figure 5.1: The schematic set up of a pulse shaper. CL_1, CL_2; cylindrical lens, G; grating, θ_i; incident angle, θ_d; diffraction angle.

the atmosphere during propagation, and gratings are placed in the Littrow configuration ($\alpha = 1$).

The assumed spatial profile of the input pulse is Gaussian with FWHM of 1 mm, and the central wavelength is 749.4 nm. Although, the light pulse generated by Ti:Sapphire laser has a sech^2-temporal profile, to reduce the computation time, we assumed a Gaussian profile with FWHM of 100 fs. The Gaussian and sech^2 profile differ imperceptibly as long as a nonlinear phenomenon does not intervene. An output Wigner distribution function is a four-dimensional (x, ξ, t, ω) distribution, thus by two-dimensionally integration, we can obtain an arbitrary two-dimensional profile of an output pulse on non-integrated axes. For numerical calculation, we used 64 sampling points along the integrated axes and 32 sampling points along the displayed axes.

The Wigner transform matrix of an ideal pulse-shaper, without any misalignment, is

$$\begin{bmatrix} x_o \\ \xi_o \\ t_o \\ \omega_o \end{bmatrix} = \begin{bmatrix} -1 & 0 & 0 & 0 \\ 0 & -1 & 0 & 0 \\ 0 & 0 & 1 & 0 \\ 0 & 0 & 0 & 1 \end{bmatrix} \begin{bmatrix} x_i \\ \xi_i \\ t_i \\ \omega_i \end{bmatrix} \tag{5.7}$$

where we assume that A = B = C = D = f = 500 mm and $G_1 = G_2$ = 600 lp/mm. The spatial component (the elements of 1-1, 1-2, 2-1 and 2-2) of the transform matrix of Eq. (5.7) create a negative unit matrix, and the temporal component (the elements of 3-3, 3-4, 4-3 and 4-4) create a positive unit matrix, so that the output electric field intensity profile equals the input profile, except that the spatial profile is inverted.

The numerically calculated output profile is shown in Fig. 5.2. In this Figure, the brighter and darker points represent higher and lower intensity. It is clear from Fig. 5.2 and Eq. (5.7) that spatio-temporal coupling is not induced by the ideal pulse-shaper.

5.3.2 A Pulse-Shaper with Defocused lenses

In this section, we consider a pulse-shaper with misalignment, whose the distance from CL_2 to G_2 is shorter than focal length of CL_2, and then the Wigner

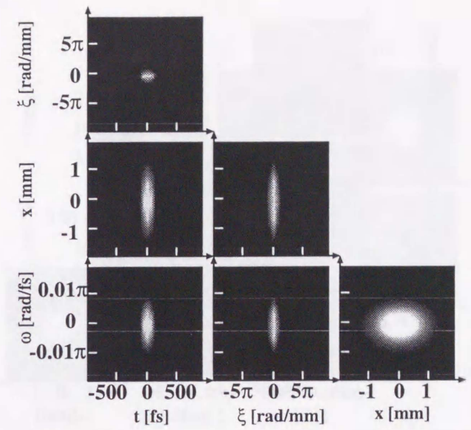

Figure 5.2: Output field intensity profile of $4f$ system. $A = B = C = D = f = 500\,mm$

transform matrix is

$$\begin{bmatrix} x_o \\ \xi_o \\ t_o \\ \omega_o \end{bmatrix} = \begin{bmatrix} -1 & -\frac{50}{k_0} & 0 & \frac{50\beta}{k_0} \\ 0 & -1 & 0 & 0 \\ 0 & \frac{50\beta}{k_0} & 1 & -\frac{50\beta^2}{k_0} \\ 0 & 0 & 0 & 1 \end{bmatrix} \begin{bmatrix} x_i \\ \xi_i \\ t_i \\ \omega_i \end{bmatrix} \tag{5.8}$$

where we assume that A = B = C = f = 500 mm , D = 450 mm and G_1 = G_2 is 600 lp/mm. In Eq. (5.8), ξ_o and ω_o are transformed to $-\xi_i$ and ω_i, respectively, x_o and t_o include ξ_i-ω_i coupling in addition to x_i and t_i. We expect the spatio-temporal coupling effect occurs. The numerically calculated output profile is shown in Fig. 5.3. We can find that the temporal delay is induced on the x-t and ω-t plot, by comparing Fig. 5.2 and Fig. 5.3.

In the temporal profile, the FWHM of the output pulse is 4.0 times longer than that of the input pulse. We can confirm that the spatio-temporal coupling induces the temporal chirp in the ξ-t, x-t and ω-t plot. According to Eq. (5.8), the spatial chirp is induced by the spatio-temporal coupling effect, although the x-ξ plot of Fig. 5.2 and Fig. 5.3 are the same. This result means that the influences of ξ_i and ω_i cancel each other out, so that the spatial profile does not come under the influence of the spatio-temporal coupling effect.

In the same way, when the distance from CL_2 to G_2 is longer than the focal length of CL_2 (that is $D > f$, if we assume that A = B = C = f = 500 mm, D = 550 mm and G_1 = G_2 is 600lp/mm), the Wigner transform matrix is represented by Eq. (5.9). In this case, the numerically calculated output profile is opposite to Fig. 5.3 with respect to the direction of the temporal chirp. The chirp direction corresponds to the sign of the elements 3-2 and 3-4 in Eq. (5.8) and Eq. (5.9).

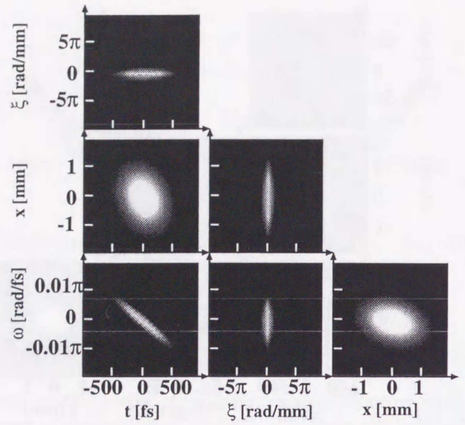

Figure 5.3: Output field intensity profile. $A = B = C = f = 500\,mm, D = 450\,mm$.

$$\begin{bmatrix} x_o \\ \xi_o \\ t_o \\ \omega_o \end{bmatrix} = \begin{bmatrix} -1 & \frac{50}{k_0} & 0 & -\frac{50\beta}{k_0} \\ 0 & -1 & 0 & 0 \\ 0 & -\frac{50\beta}{k_0} & 1 & \frac{50\beta^2}{k_0} \\ 0 & 0 & 0 & 1 \end{bmatrix} \begin{bmatrix} x_i \\ \xi_i \\ t_i \\ \omega_i \end{bmatrix} \tag{5.9}$$

As shown in Fig. 5.4 by comparing the intensity profile of cases $D < f$ and $D > f$, the x-t plot is the same and the t-ω plot varies its inclination. The former case shows that the chirp direction of the temporal and spatial profile are inverted by the spatio-temporal coupling effect, and the latter case shows the direction of the temporal chirp to be inverted. Therefore, we can find that high frequency components are forwarded in the case of $D < f$ whereas in the other case the low frequency components are forwarded.

5.3.3 A Pulse-Shaper with Different Grating Constants

In this section, we consider a pulse-shaper whose input and output grating have different grating constants, without misalignment. The Wigner transform matrix is then

$$\begin{bmatrix} x_o \\ \xi_o \\ t_o \\ \omega_o \end{bmatrix} = \begin{bmatrix} -1 & 0 & 0 & 0 \\ 0 & -1 & 0 & \beta_1 - \beta_2 \\ \beta_2 - \beta_1 & 0 & 1 & 0 \\ 0 & 0 & 0 & 1 \end{bmatrix} \begin{bmatrix} x_i \\ \xi_i \\ t_i \\ \omega_i \end{bmatrix} \tag{5.10}$$

where we assume that $A = B = C = D = 500\,mm$, G_1 is 600 lp/mm and G_2 is 1200 lp/mm, $\beta_1 = 2\pi/(d_1\omega_0 \cos\theta_{d_1})$ and $\beta_2 = 2\pi/(d_2\omega_0 \cos\theta_{d_2})$ are defined by

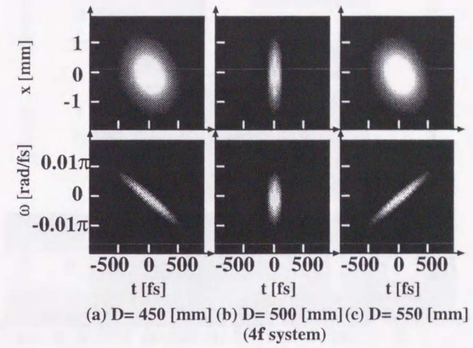

Figure 5.4: Output field intensity profile. (a) $D = 450\,mm$; (b) $D = 500\,mm$; (c) $D = 550\,mm$.

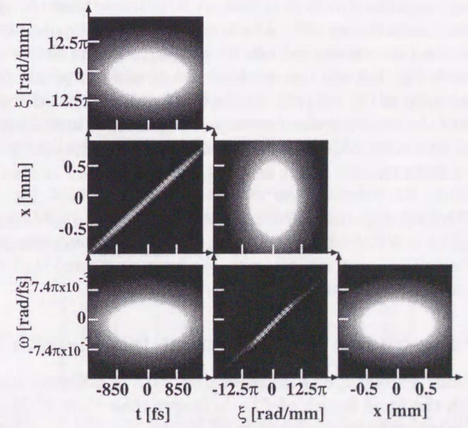

Figure 5.5: Output field intensity profile. ($A = B = C = D = f = 500\,mm$, $G_1 : 600\,lp/mm$, $G_2 : 1200\,lp/mm$)

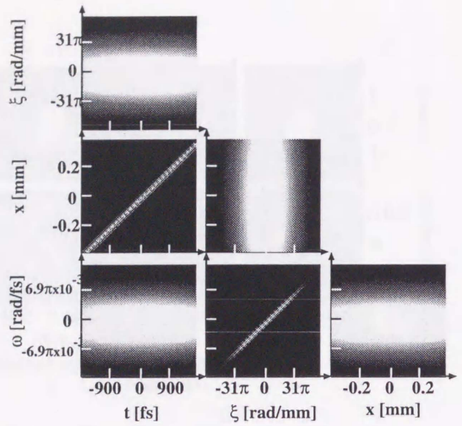

Figure 5.6: Output field intensity profile. ($A = B = C = D = f = 500\,mm$, $G_1 : 600\,lp/mm$, $G_2 : 1800\,lp/mm$)

several grating constants $d_1 = 1/600\,mm$ and $d_2 = 1/1200\,mm$. In Eq. (5.10), x_o and ω_o are transformed to $-x_i$ and ω_i, respectively, ξ_o and t_o include ξ_i-ω_i and t_i-x_i coupling in addition to ξ_i and t_i. We can see that the spatio-temporal coupling effect induces the chirp at the spatial frequency and temporal profile. In this case, the numerically calculated output profile is shown in Fig. 5.5. As compared with Fig. 5.7, we can see that the spatio-temporal coupling induces the temporal chirp in the x-t plot. In the temporal and spatial frequency profile, the FWHM of the output pulse stretches 15.4 and 8.8 times longer respectively as a result of this chirp. Also, we have confirmed that the light pulse shifts from upward to downward.

In addition, by reducing the output grating constant ($d_1 = 1/600\,mm$、$d_2 = 1/1800\,mm$), the numerically calculated output profile varies as shown in Fig. 5.6. The FWHM of the temporal and spatial frequency profile stretches 44 and 20 times the input respectively. We have confirmed that the quantity of the chirp increases when reducing the grating constant.

5.3.4 Pulse-Shaper with different focal length lens pair

In this section, we consider a pulse-shaper with a different focal length lens pair in which the focal length of CL_1 is longer than that of CL_2. The Wigner transform matrix then takes the form of

$$\begin{bmatrix} x_o \\ \xi_o \\ t_o \\ \omega_o \end{bmatrix} = \begin{bmatrix} -\frac{4}{5} & 0 & 0 & 0 \\ 0 & -\frac{5}{4} & 0 & \frac{\beta}{4} \\ -\frac{\beta}{5} & 0 & 1 & 0 \\ 0 & 0 & 0 & 1 \end{bmatrix} \begin{bmatrix} x_i \\ \xi_i \\ t_i \\ \omega_i \end{bmatrix} \tag{5.11}$$

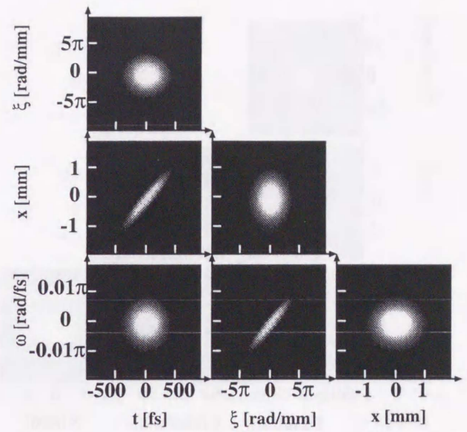

Figure 5.7: Output field intensity profile. $A = B = 500\,mm$, $C = D = 400\,mm$.

where A = B = 500 mm, C = D = 400 mm and $G_1 = G_2 = 600$ lp/mm. In Eq. (5.11), ω_o and x_o are transformed to ω_i and $-4x_i/5$, respectively, ξ_i and t_i include ξ_i-ω_i and t_i-x_i in addition to ξ_i and t_i. The numerically calculated output profile is shown in Fig. 5.7. As compared with Fig. 5.2, the ξ-t, ω-t and ω-ξ plot are spread by the chirp of the temporal and spatial frequency profile. In the x-t and ω-ξ plot, both the temporal and temporal frequency chirp are induced by the spatio-temporal chirp. The light pulse is moved along the spatial axis by the temporal chirp. The FWHM of the temporal and spatial profile stretch 3.2 and 4.0 times the input pulse respectively. On the other hand, the FWHM of the spatial profile is compressed by a factor of 0.8 times since x_o is in proportion to the focal length ratio and is smaller than x_i, as shown in Eq. (5.11).

In the same way, when the focal length of CL_2 is longer than CL_1 (we assume A = B = 500 mm and C = D = 600 mm, that is, $A < C$), the Wigner transform matrix is

$$\begin{bmatrix} x_o \\ \xi_o \\ t_o \\ \omega_o \end{bmatrix} = \begin{bmatrix} -\frac{6}{5} & 0 & 0 & 0 \\ 0 & -\frac{5}{6} & 0 & -\frac{\beta}{6} \\ \frac{\beta}{5} & 0 & 1 & 0 \\ 0 & 0 & 0 & 1 \end{bmatrix} \begin{bmatrix} x_i \\ \xi_i \\ t_i \\ \omega_i \end{bmatrix} \tag{5.12}$$

According to Eq. (5.12), the sign of the element of 2-4 and 3-1 differs from that in Eq. (5.11). We can see that the direction of the chirp is reversed. In this case, the numerically calculated output profile is shown in Fig. 5.8. We can confirm that the direction of the chirp is opposite to case $A > C$ by comparing Fig. 5.7 and Fig. 5.8. The inclination of the x-t and ω-ξ plot are also varied by the spatio-temporal chirp. The FWHM of the temporal, spatial frequency and spatial profile stretch 3.2, 2.7 and 1.2 times of the input pulse, respectively. The

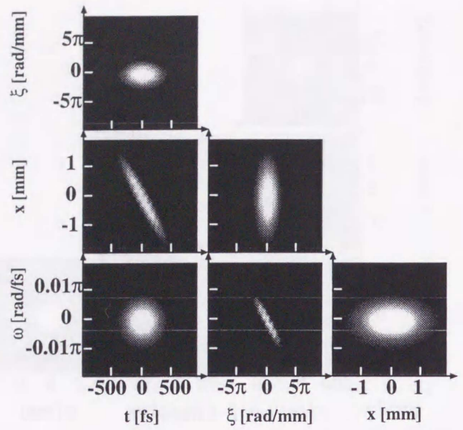

Figure 5.8: Output field intensity profile. $A = B = 500\,mm$, $C = D = 600\,mm$.

FWHM of spatial frequency profile is narrower than the case $A > C$, because the element of 2-2, the in proportion to ξ_i is smaller than 1.

A comparison of cases $A > C$ and $A < C$ shows that the FWHM of the spatial profile is proportional to the focal length ratio. The magnification of the FWHM is decided by the focal length ratio, that is, A/C. The chirp direction of ξ and t are inverted by the magnification, and the inclination of the x-t and ω-ξ plot also vary. The FWHM of the spatial frequency profile is changed by the spatio-temporal chirp, although the FWHM of the temporal profile remains the same. According to Eq. (5.12), the absolute value of elements 3-1 and 3-3 is the same, although elements 2-2 and 2-4 is different, so that the spatial frequency profile is changed. As a result of the temporal chirp, the top and tail of the pulse arrive at different places. When the focal length ratio is smaller than 1, we can confirm the light pulse moves along the spatial axis.

5.3.5 Pulse-Shaper with different grating constants and focal length lens pair

In this section, we consider a pulse-shaper with different grating constants and focal length lens pair whose the Wigner transform matrix is

$$\begin{bmatrix} x_o \\ \xi_o \\ t_o \\ \omega_o \end{bmatrix} = \begin{bmatrix} -\frac{6}{5} & 0 & 0 & 0 \\ 0 & -\frac{5}{6} & 0 & \frac{5}{6}\beta_1 - \beta_2 \\ \frac{6}{5}\beta_2 - \beta_1 & 0 & 1 & 0 \\ 0 & 0 & 0 & 1 \end{bmatrix} \begin{bmatrix} x_i \\ \xi_i \\ t_i \\ \omega_i \end{bmatrix} \tag{5.13}$$

where A = B = 500 mm, C = D = 600 mm, G_1 is 600 lp/mm and G_2 is 1200 lp/mm. As compared with Eq. (5.12), the quantity of the chirp is a function of the grating constant ratio of the grating-pair. The numerically calculated

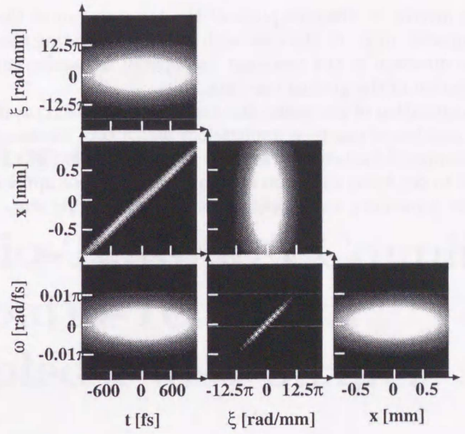

Figure 5.9: Output field intensity profile. ($A = B = 500\,mm, C = D = 600\,mm$, $G_1 : 600\,lp/mm$, $G_2 : 1200\,lp/mm$)

output profile is shown in Fig. 5.9. A comparison of Fig. 5.9 with Fig. 5.8 shows the direction of the spatio-temporal chirp to be opposite in the x -t and/or ω-ξ plot. The FWHM of the temporal and spatial frequency profile of the output pulse are stretched to 15.1 and 6 times respectively that of the input pulse by the spatio-temporal chirp.

For the above result, the spatial profile can be controlled by the focal length ratio, and the direction of the spatio-temporal chirp is possible to be controlled by the addition of grating-pairs with different grating constants.

5.4 Summanry

In this chapter, we numerically analyzed the spatio-temporal properties of several pulse-shapers, specifically an ideal pulse-shaper, a pulse-shaper with lens defocus, with a grating-pair with different grating constant, with a lens-pair with different focal lengths and combinations of these using the Wigner distribution function.

In the case of lens defocus, we have confirmed that the spatio-temporal coupling effect induces a temporal chirp, and the velocity of the temporal frequency component is varied by the chirp. In addition, if the displacement of the distance from CL_2 to G_2 is the same, the spatio-temporal distribution is the same and not dependent on the distance. In the case with different grating constants, the degree of both the temporal and spatial frequency chirp is varied by combination of different grating constants, and the light pulse is moved on the spatial axis by the temporal chirp. In the case of different focal length lenses, the FWHM of the spatial profile is in proportion to focal length ratio, and the

light pulse arrives at different place of the top and tail of the pulse induced by the temporal chirp. In the case with a different grating constant and focal length, the direction of the temporal and spatial frequency chirp is varied by the combination of the grating constant.

The quantization of the spatio-temporal coupling effect, as described above, suggests a number of practical applications which take advantage of the effects of specific temporal frequency on arbitrary spatial position which enable changes to be made to the beam direction of a light pulse. These applications will have potential for controlling the properties of high speed solid state components.

Chapter 6

Spatio-Temporal Coupling in Spatio-Temporal Coupled Pulse Shaper

An improved pulse shaper is proposed which is able to control both the spatial and temporal profile of femtosecond light pulses. Our pulse shaper exploits the spatio-temporal coupling effect seen in pulse shapers. Its properties are numerically analyzed by application of the Wigner distribution function. We confirm that the spatio-temporal output pulse track dictates the differentiation of the phase mask; that the degree of spatio-temporal coupling is determined by the focal length ratio of the lenses in the pulse shaper; and that space to spatial-frequency chirp results from misalignment of lenses.

6.1 Introduction

A femtosecond light pulse has a number of interesting and useful properties which result from its short temporal duration. Many potential applications of these properties, such as the control and measurement of the ultrafast properties of materials, and high capacity, high speed communications have been studied[44, 4, 45].

To realize these applications, the key issue is how to control the temporal profile of a femtosecond light pulse with high accuracy; and to realize such control, spectral modulating pulse shaping techniques are being intensively studied[2, 36]. In this method, the broad temporal spectrum of a femtosecond light pulse is spread spatially by means of a grating-lens pair and then modulated using a spatial light modulator (SLM) or the like. The spectrum is then re-Fourier transformed into a temporal signal using another grating-lens pair. The optical setup for this operation is called a pulse shaper.

In a pulse shaper or a spectrometer, it is impossible to avoid spatio-temporal coupling effects as mentioned in chapter 5[47, 48]. As a result of diffraction, the temporal profile of an electric field is influenced by its former spatial profile. Similarly, the spatial profile of an electric field is influenced by its previous temporal profile. In some applications, spatio-temporal coupling creates a number

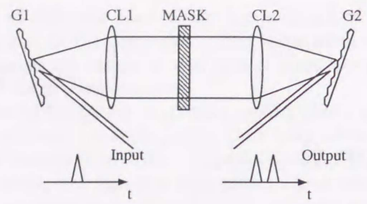

Figure 6.1: The schematic setup of a conventional pulse shaper. CL denotes cylindrical lens, and G grating.

of problems, such as spatial and/or temporal defocus or spatial and/or temporal chirp. For example, in a pulse shaper or a spectrometer, this coupling can be ignored if the spatial beam shape is sufficiently wider than its temporal version[49].

On the other hand, if a convoluted spatio-temporal axis can be generated by coupling, employing this axis makes it possible to simultaneously control the temporal and spatial axis of a femtosecond light pulse by means of one-dimensional modulation. Some pulse shapers, however, apply coupling and control pulses both spatially and temporally, but use only spontaneous spatio-temporal coupling. We have proposed a spatio-temporally coupled pulse shaper (STCPS), which artificially enhances spatio-temporal coupling and controls the temporal and spatial profile of a femtosecond light pulse simultaneously by means of a one-dimensional spatial light modulator (SLM)[50].

In this chapter, we analyze the STCPS by using the spatio-temporal Wigner distribution function[51, 52]. This approach allows the entire optical system to be described as one simple coordinate transform matrix, dramatically reducing the amount of calculation required for numerical analysis.

6.2 Spatio-Temporally Coupled Pulse Shaper

The schematic setup of a conventional pulse shaper is shown in Fig. 6.1. The spectrum of an input light pulse is spatially spread by means of a grating-lens pair, G1-CL1, then modulated by a mask, which may be a liquid crystal SLM or the like. Finally, the temporal light pulse is reconstructed by another grating-lens pair, G2-CL2. This setup enables the rapidly varying temporal profile of the pulse to be controlled in spite of the use of a slow-response modulating device.

The field amplitude of the input pulse is assumed to be $E_0(x_0, t_0)$:

$$E_0(x_0, t_0) = E_0^S(x_0)E_0^T(t_0) \tag{6.1}$$

where $E_0^S(x_0)$ and $E_0^T(t_0)$ are the temporal and spatial profile of $E_0(x_0, t_0)$, respectively and x_0 and t_0 are spatial and temporal variables on the input plane. The input pulse is Fourier transformed by the grating-lens pair, and the

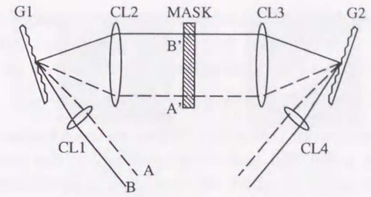

Figure 6.2: The schematic setup of a spatio-temporally coupled pulse-shaper. CL1 CL4 denote spatio-temporal coupling lenses with focal length of f_c. CL2 and CL4 denotes shaper-lenses with focal length of f_s. G is grating.

field amplitude on the mask plane is expressed as

$$E_1(x_1, t_1) = \hat{E}_0^S(x_1) * \tilde{E}_0^T(t_1) \tag{6.2}$$

where $\hat{E}_0^S$ and $\tilde{E}_0^T$ are the spatial and temporal Fourier transforms of $E_0^S(x_0)$ and $E_0^T(t_0)$, respectively. According to this equation, the field amplitude on the mask plane is a convolution of the temporal Fourier transform of $E_0^T(t_0)$ and the spatial Fourier transform of $E_0(x_0)$. This convolution takes the form of spatio-temporal coupling. In most cases, the temporal duration of the pulse is sufficiently shorter than the spatial duration, as in

$$\mathcal{W}\left[\tilde{E}_0(x_0, \omega_0)\right] >> \mathcal{W}\left[\hat{E}_0^S(\xi_0, t_0)\right], \tag{6.3}$$

where $\mathcal{W}[f(\mu)]$ corresponds to the width of $f(\mu)$; $\tilde{E}_0(x_0, \omega_0)$ and $\hat{E}_0^S(\xi_0, t_0)$ are the temporal and spatial Fourier transforms of $E_0(x_0, t_0)$, respectively; and ξ_0 and ω_0 are the spatial and temporal frequency on the input plane. We can regard $\hat{E}_0^S$ as a delta function, thus allowing spatio-temporal coupling to be ignored. Hence, the spatial pulse profile on the mask equals its temporal spectral profile.

On the other hand, our STCPS enhances spatio-temporal coupling, and employs coupling to simultaneously control both the temporal and spatial profile of the light pulse. Figure Figure 6.2 shows the schematic setup of the STCPS. CL1 and CL4 are spatio-temporal coupling lenses which induce spatio-temporal coupling and whose focal lengths are represented by fc; and CL2 and CL3 are pulse shaper lenses of focal length fs. In this system, the input pulse is spatially Fourier transformed by CL1 before the grating G1. The condition shown in eq. (6.3) thus cannot be satisfied. The electric field profile on the mask plane is determined as the convolution of the spatial profile and temporal spectral profile of the input light pulse. We will explain the properties of the system quantitatively and numerically by use of the Wigner function later, but we will explain it here intuitively and geometrically.

Light beams which pass along the dashed beam line and the solid beam lines in Fig. 6.2 have different incident angles to the grating, with the result that their spectral components are spread on different areas on the mask. By taking advantage of this property, we can modulate the temporal profiles of the beams independently using one-dimensional SLM; in other words, we can simultaneously control the spatial and temporal profile of the pulse.

In accordance with the shift-law of Fourier transforms, when the temporal spectrum $\hat{E}(\omega)$ is modulated by a linear phase bias, the temporal profile is shifted in proportion to the inclination of the phase as in

$$\mathcal{F}[\hat{E}(\omega)\exp(i2\pi a\omega)] = E(t+a), \tag{6.4}$$

where $\mathcal{F}$ refers to Fourier transform. When we use a phase-only mask in STCPS, the output light pulse will shift in proportion to the phase inclination of the small part of the mask at which the spectrum is modulated. Hence, the spatial differentiation pattern of the phase-mask appears on the output spatio-temporal plane[53].

6.3 Wigner Expression of Spatio-Temporally Coupled Pulse-Shaper

The STCPS is constructed of elements which are described by eq. (5.2), eq. (5.3) and eq. (5.4) and a phase-mask. The transform matrix of the STCPS can thus be obtained as the crossproducts of element-matrixes. The transform matrix between the input plane and the phase-mask plane of the STCPS is

$$\begin{bmatrix} -f_s/(\alpha f_c) & 0 & 0 & \beta f_s/(\alpha k_0) \\ 0 & -\alpha f_c/f_s & 0 & 0 \\ 0 & \beta f_c/k_0 & 1 & 0 \\ 0 & 0 & 0 & 1 \end{bmatrix} \tag{6.5}$$

On the other hand, the same matrix for a conventional pulse shaper is

$$\begin{bmatrix} 0 & -f_s/(\alpha k_0) & 0 & \beta f_s/(\alpha k_0) \\ \alpha k_0/f_s & 0 & 0 & 0 \\ -\beta & 0 & 1 & 0 \\ 0 & 0 & 0 & 1 \end{bmatrix} \tag{6.6}$$

The first rows of eq. (6.5) and (6.6) represent the effect of the input pulse profile on the output spatial x profile. In eq. (6.6), the case of an ordinary pulse shaper, element 1-1 is 0 and element 1-2 is $-f_s/(\alpha k_0)$, so that the spatial output profile is determined by the ξ and ω profile of the input pulse. The spatial profile on the mask plane is a convolution of the ξ and ω profile of the input, and in most cases the ξ profile can be regarded as a delta function, meaning that the spatial profile can be regarded for practical purposes as a profile of the input pulse.

On the other hand, in the case of the STCPS described in eq. (6.5), the spatial profile on the mask plane is determined by the x and ω profile of the input. Normally, the width of the x profile is much greater than that of ξ, so we should regard the spatial profile on the mask plane as the convolution of the x and ω profile of the input. This convolution causes spatio-temporal coupling, and the significance of the coupling is controllable by changing the focal length ratio of f_s and f_c, because element 1-1 of the matrix is $-f_s(-\alpha f_c)$.

6.4 Numerical Analysis

In this section, we numerically analyze the behavior of the STCPS with a number of phase-masks. We base our calculations on the optical setup illustrated in

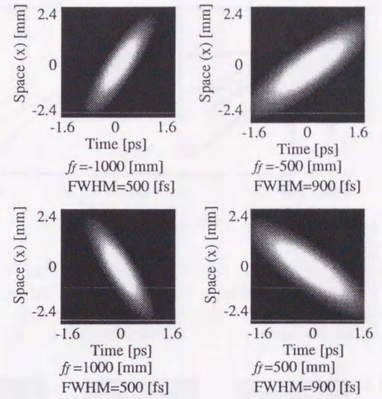

Figure 6.3: Spatio-temporal profile of output light pulse of STCPS with quadratic phase-masks.

Fig. 6.2. The spatial and temporal FWHM of the input light pulse are 100 fs and 2.0 mm, respectively, and its central wavelength is 775 nm.

6.4.1 STCPS with Quadratic Phase-Mask

The phase mask is assumed to be a cylindrical lens which can also be regarded as a quadratic phase mask. We assume all the focal lengths of CL1, CL2, CL3 and CL4 to be 50 mm and the grating constant of G1 and G2 to be 2000 lp/mm. First, we analytically calculated the transform matrix of the optical setup, then numerically calculated the output light profiles in 32×32 pixel squares as shown in Fig. 6.3. The focal lengths of the cylindrical lenses for the phase masks f_f are -1000 mm, -500 mm, 500 mm and 1000 mm. The output spatio-temporal pulse profile should thus be a derivative of the phase mask, putting the time-space inclinations of the output pulses in proportion to the focal length of the mask-lenses. Their temporal FWHMs are 500 fs, 500 fs, 900 fs and 900 fs, respectively, and are in inverse proportion to the focal length of the mask-lenses.

6.4.2 STCPS with Cubic Phase Mask

Now we assume cubic phase masks as shown in Fig. 6.4; (a) $\phi(x) = 4.5\times10^{-8}x$, (b) $\phi(x) = 3.5\times10^{-8}x$ and (c) $\phi(x) = 2.5\times10^{-8}x$, where x mm is spatial position on the phase-mask and ϕ radian is phase-modulated by the phase-mask. We assume that the focal lengths of CL1 and CL4 are 20 mm and those of CL2 and CL3 are 130 mm, respectively, and the grating constants of G1 and G2 are 2000 lp/mm. It can be confirmed that the output spatio-temporal pulse

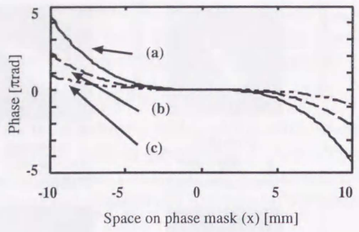

Figure 6.4: Cubic phase masks, (a) $\phi(x) = 4.5 \times 10^{-8}x$, (b) $\phi(x) = 3.5 \times 10^{-8}x$ and (c) $\phi(x) = 2.5 \times 10^{-8}x$, where the unit of x is milimeter and unit of ϕ is radian.

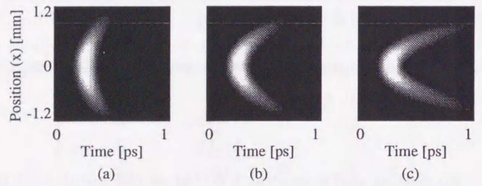

Figure 6.5: Spatio-temporal profiles of output light pulse. It can be confirm that the spatio-temporal peak tracks forms quadratic curves.

profiles form quadratic curves as in

$$T(x) = 0.41 \times 10^{-3}x^2 \tag{6.7}$$
$$T(x) = 1.01 \times 10^{-3}x^2 \tag{6.8}$$
$$T(x) = 1.90 \times 10^{-3}x^2 \tag{6.9}$$

by Fig. 6.5, where $T(x)$ means the temporal position of the output pulse peak on each x. Equation (6.7), (6.8) and (6.9) correspond to the cases of (a), (b) and (c) in Figs. 6.4 and 6.5. These equation are calculated using the least squares method, from the numerically analyzed results. The root-mean-squared errors (RMS) of (a), (b) and (c) are 0.19×10^{-3} ps, 3.67×10^{-3} ps and 12.52×10^{-3} ps, respectively. A larger curvature of the phase-mask results in a larger RMS, with the errors localized in the spatial outer side of the output pulse.

6.4.3 Effect of Focal Length Ratio between Coupling and Shaping Lens

Equation (6.6) indicates that the coefficient of spatio-temporal coupling of STCPS is determined by the focal length-ratio of the spatio-temporal coupling lenses CL1 and CL4 to that of the pulse shaper lenses CL2 and CL3. We numerically calculated several output pulse profiles using different combinations of

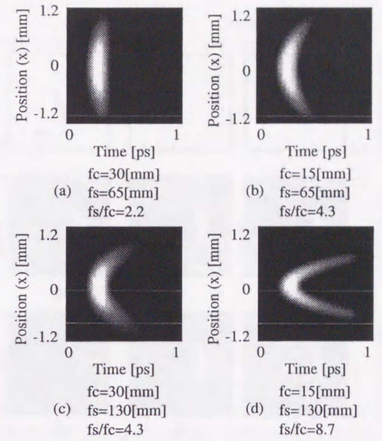

Figure 6.6: Spatio-temporal profile of output light pulse with come combination of focal length ratio of spatio-temporal coupling lenses, f_c to pulse-shaper lens, f_s.

focal lengths, as shown in Fig. 6.6. A larger focal length ratio f_c of the coupling lens to that of the shaper lens f_s creates a higher degree of spatio-temporal coupling. Although in the cases of (b) and (c), the focal length ratio is the same, $f_s/f_c = 4.3$, the output pulses have a different curvature. This is because eq. (6.6) dictates that the spatio-temporal coupling effect is determined by both the focal length ratio and the f_s to the central wavelength ratio, as shown in the 1-4 element in eq. (6.6).

6.4.4 Effect of Defocus of Coupling Lens

Figure 6.7 shows the output pulse profiles in the case of an STCPS with defocused CL1. Columns (a), (b) and (c) show, respectively, cases where the distance between CL1 and G1 is 20% shorter than the focal length of CL1; is at the focal length; and is 20% longer than the focal length. The pictures on the second row show that the spatio-temporal intensity profile is the same on the output plane, although ξ-x chirp is present in proportion to the degree of defocus. Due to the effects of chirp, the spatio-temporal profiles are developed into different forms with spatial propagation. After 8 cm propagation, the spatial profiles of (a) and (c) are respectively broader and narrower than that of (b).

6.5 Summary

In this chapter, we have proposed a spatio-temporally coupled pulse shaper (STCPS) for simultaneous spatial and temporal control of ultra fast light pulses

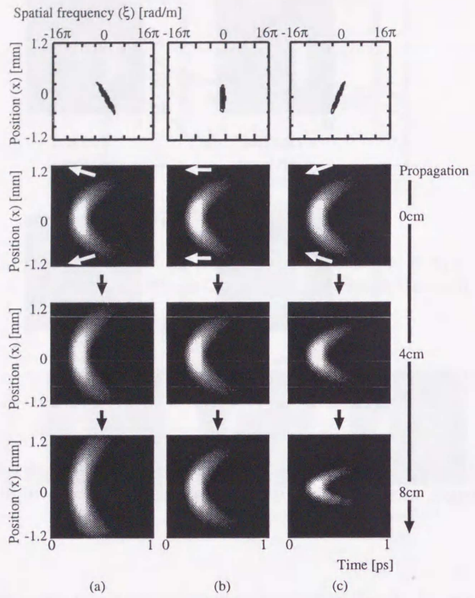

Figure 6.7: Spatio-temporal profile of output light pulse with misalignment of a coupling lens. The distance between CL1 and G1 is (a) 20% shorter than the focal length of CL1, (b) the focal length and (c) 20% longer than the focal length. The first line shows the ξ-x distributions on output plane, and others shows t-x distributions.

by means of one-dimensional spatial light modulation.

We have numerically analyzed the spatio-temporally coupled pulse shaper (STCPS) using the Wigner distribution function, which affords a dramatic reduction in the amount of calculation required to describe spatio-temporal coupling in comparison with the ordinary method based on complex amplitude. Several behaviors of the STCPS were confirmed. Quadratic phase modulation by means of a lens causes the spatio-temporal pulse track to form a line whose inclination is in proportion to the focal length of the modulating lens. Cubic phase modulation results in the spatio-temporal pulse track forming a curve of second degree whose second order coefficient is in proportion to the third order coefficient of the phase-mask. The influence of spatio-temporal coupling is controlled by the focal length ratio of coupling lenses to shaper lenses and the wavelength of the light source to the focal length of the shaper lens. x-ξ chirp occurs as a result of defocusing the coupling lens, although the x-t intensity profile on the output plane remains constant.

Chapter 7

Time-Domain Microscope

7.1 Introduction

Direct measurement of ultrafast light pulse is currently limited to several hundread femtosecond resolution based on the performance of state-of-art photodetectors, oscilloscopes, and streak cameras. To extend the direct measurement capability, Bennett *et al.* have developped a technique of a time-microscope[55]. Based on the anologies between dispersion and freespace diffraction, and quadratic phase modulation and a lens[12], the time-microscope achives in the time domain what microscopes achive in space.

In this chapter, we numerically analyze the the spatio-temporal property of a time-microcope by using Wigner distribution function.

7.2 Priciple of Time-Domain Microscope

The schematic setup of temporal imaging system is shown in Fig. 7.1. An input pulse enters the time-microscope and is dispersed by an input grating pair by spectral quadratic phase

$$\tilde{E}_2(\omega) = \tilde{E}_1(\omega) \times \exp\left(-i\frac{\beta_{11}^2 z_1}{\alpha_{11}^2 k_0}\omega^2\right) \tag{7.1}$$

where $\tilde{E}_1$ and $\tilde{E}_2$ are temporal Fourier transform of input pulse $E_1(t)$ and output pulse $E_2(t)$ of the grating-pair, α_{11} and β_{11} the parameter of the gratings which are defined as $\alpha_{11} = \cos\theta_{11}/\cos\theta_d$, $\beta_{11} = 2\pi mN/(\omega_0 \cos\theta_d)$ when θ_i and θ_d are incident and diffraction angle of the first grating (G11), Nlp/mm is the grating constant, m is diffraction-order and ω_0 is the central frequency of the pulse. The second grating (G12) is placed as $\alpha_{12} = 1/\alpha_{11}$ and $\beta_{12} = \beta_{11}/\alpha_{11}$. The pulse next encounters a temporal puadratic phase modulation process, in some implementations, which is approximatelly achived by co-sinusoidal modulation.

$$E_3(t) = E_2(t) \times \exp\left(i\frac{\omega_0}{2f_T}t^2\right) \tag{7.2}$$

where f_T is focal time. Finally, the pulse is dispersed again by the second grating-pair as the same of eq. (7.1).

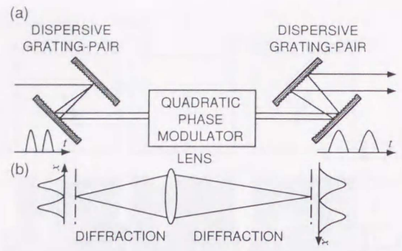

Figure 7.1: Schematic setup of (a) temporal and (b) spatial imaging system. Input and output grating pairs in (a) make spectral dispersion which accordance with the free-space dispersion in (b), and quadratic phase modulator act as a time-lens.

The spatial one-dimensional Fresnel diffraction is expressed as

$$E_{out}(\xi) = E_{in}(\xi) \times \exp\left(-i\frac{z_f}{k_0}\xi^2\right) \tag{7.3}$$

where ξ is spatial frequency, z_f is propagation distance. Equation (7.1) and eq. (7.3) have the same form, so that the dispersion of the grating pair can be regard as temporal Fresnel diffraction whose diffraction length is

$$\tau_1 = \beta_{11}^2 z_1/\alpha_{11}^2. \tag{7.4}$$

The effect of a spatial one-dimensional lens is expressed as

$$E_{out}(x) = E_{in}(x) \times \exp\left(i\frac{ik_0}{2f_S}x^2\right) \tag{7.5}$$

Equation (7.2) and eq. (7.5) have the same shape, so that the temporal quadratic phase modulation can be regard as temporal lens that is sometime called time lens, and f_T is sometime called focal time[12].

These analogies provide a temporal imaging condition as

$$\frac{1}{\tau_1} + \frac{1}{\tau_2} = -\frac{1}{f_T} \tag{7.6}$$

where τ_2 is the temporal Fresnel diffraction distance of the second grating-pair. When eq. (7.6) is satisfied, the time-microscope expands the temporal input signal by a magnification factor

$$M = -\frac{\tau_2}{\tau_1}. \tag{7.7}$$

7.3 Wigner Expression of Time-Microscope

The time-microscope is constructed by elements which expressed by eq. (5.2), eq. (5.3) and eq. (5.4), so that its tranform matrix is calculated by the crossproducts of the element-matrixes as

$$\left[\begin{array}{cc:cc} 2M-1 & 0 & \frac{1-M}{\beta} & -\frac{2f_T(1-M)}{\beta k_0} \\ \frac{4\beta^2 k_0}{f_T} & \frac{2}{M}-1 & -\frac{2\beta k_0}{f_T} & -\frac{2\beta(1+M)}{M} \\ \hdashline -2\beta(M+1) & -\frac{2f(M-1)}{M\beta k_0} & M & \frac{2f_T(M-1)^2}{Mk_0} \\ -\frac{2\beta k_0}{f_T} & \frac{M-1}{\beta M} & \frac{k_0}{f_T} & \frac{1}{M} \end{array}\right] \tag{7.8}$$

where $\beta = \beta_{11} = \beta_{21}$, and assuming the retrow configuration, $\alpha_{11} = \alpha_{21} = 1$. The four elements on the right-up side of eq. (7.8) express time-to-space coupling, and four elements in left-low side express space-to-time coupling in the time-microscope.

To simplify the matter, we disscuss about the condition $M = 1$. The transform matrix is

$$\begin{bmatrix} 1 & 0 & 0 & 0 \\ 4\beta^2 k_0/f_T & 1 & -2\beta k_0/f_T & -4\beta \\ -4\beta & 0 & 1 & 0 \\ -2\beta k_0/f_T & 0 & k_0/f_T & 1 \end{bmatrix}. \tag{7.9}$$

The 1-3 element of eq. (7.9) is -4β, not 0, so that the output spatial profile is influenced by the input temporal profile, even though the magnification M is 1. In the following section, we numrically investigate the effect of the spatio-temporal coupling.

7.4 Numerical Analysis

In this section, we numerically analyze the behavior of the time-domain microscope with some a number of phase-masks. We base our calculations on the optical setup illustrated in Fig. 7.2. The amplitude of the co-sinusoidal phase modulation is π rad, its frequency is 18.9 KHz, the separation of the gratings of a grating pair is 15.0 cm, grating constant is 2000 lp/mm, incident angle of the grating is 50.8 deg, and these gratings are set in Littrow configuration. The input pulses have temporal and spatial FWHM of 100 fs and 1.0 mm, respectively.

7.4.1 Spatio-Temporal Coupling Induced by Magnification Changing

At the first analysis, we investigate about the spatio-temporal coupling induced by changing the magnitude of the time-domain microscope. The Wigner trans-

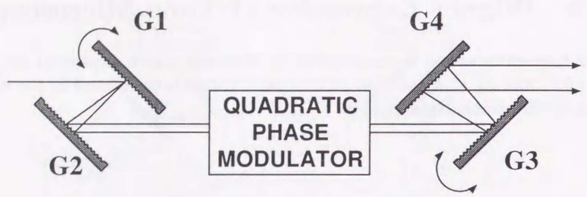

Figure 7.2: The schematic setup of analyzed time-domain microscope. The amplitude of the co-sinusoidal phase modulation is π rad, its frequency is 18.9 KHz, the separation of the gratings of a grating pair is 15.0 cm, grating constant is 2000 lp/mm, incident angle of the grating is 50.8 deg, and these gratings are set in Littrow configuration. The input pulses have temporal and spatial FWHM of 100 fs and 1.0 mm, respectively.

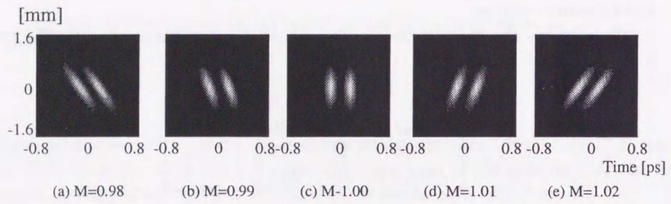

Figure 7.3: Spatio-temporal coupling indeuced by maginification changing. The magnifications are (a) $M = 0.98$, (b) $M = 0.99$, (c) $M = 1.00$, (d) $M = 1.01$, and (e) $M = 1.02$. Spatio-temporal coupling which is in propotion to the magnification is found in output spatio-temporal pulse profiles.

form matrix is

$$\begin{bmatrix} x_o \\ \xi_o \\ t_o \\ \omega_o \end{bmatrix} = \begin{bmatrix} 2M-1 & 0 & \frac{(1-M)}{\beta} & \frac{2f_T(1-M)}{\beta k_0} \\ \frac{4\beta^2 k_0}{f_T} & \frac{2}{M}-1 & -\frac{2\beta k_0}{f_T} & -\frac{2\beta(1+M)}{M} \\ -2\beta(M+1) & -\frac{2f_T(M-1)}{M\beta k_0} & M\frac{2f_T(M-1)^2}{Mk_0} & \\ -\frac{2\beta k_0}{f_T} & \frac{M-1}{\beta M} & \frac{k_0}{f_T} & \frac{1}{M} \end{bmatrix} \begin{bmatrix} x_i \\ \xi_i \\ t_i \\ \omega_i \end{bmatrix}. \tag{7.10}$$

Its 1-3 and 1-4 elements, which represent spatio-temporal coupling are 0 when $M = 1$, however, $M \neq 1$, the elements are not 0. Thet means that the spatio-temporal coupling occurs with $M \neq 1$. The numerically calculated output spatio-temporal profiles are shown in Fig. 7.3. The magnifications are (a) $\times 0.98$, (b) $\times 0.99$, (c) $\times 1.0$, (d) $\times 1.01$, and (e) $\times 1.02$. We find spatio-temporal coupling which are in propotion to the magnification, M.

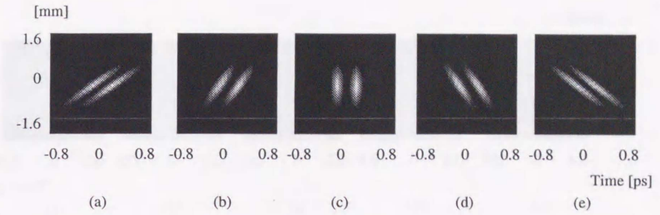

Figure 7.4: Spatio-temporal copuling induced by focal time error. The maginification M is 1.0, the frequency of the phase modulation, a time lens, ω_m is 18.9 Hz, and the ideal amplitude of modulation A_Φ is 1.0π rad. The errors are (a) -2%, (b) -1%, (c) 0%, (d) +1%, and (e) +2%.

7.4.2 Spatio-Temporal Coupling Induced by Focal Time Error

We investigate about the spatio-temporal copuling in the case of the focal time of a time lens, the amplitude of phase modulation of a phase modulator A_Φ, changes. The situation corresponds to the case of focal length miss-alignment of a spatial imaging system. By the focal time error, spatio-temporal coupling is induced even if the magnification M=1.0. The numerically calculated output pulse profiles are shown in Fig. 7.4. In this case, the ideal amplitude of phase modulation is determined as π rad, and the phase modulation frequency ω_m=18.9 Hz. In the calculation, -2% to +2% errors, (a) $A_\Phi = 0.98\pi$ rad, (b) $A_\Phi = 0.99\pi$ rad, (c) $A_\Phi = 1.00\pi$ rad, (d) $A_\Phi = 1.01\pi$ rad, and (e) $A_\Phi = 1.02pi$ rad, are appliyed to the modulation. We confirm that the degree of spatio-temporal coupling is in proportion to the quantity of the focal time error.

7.4.3 Spatio-Temporal Coupling Induced by Propagation Time Error

As same as the case of focal time error, shown in section 7.4.2, spatio-temporal coupling is induced by the propagation time error of the first grating-lens pair, even if the magnification $M = 1.0$. The numerically calculated spatio-temporal output profiles in this case are shown in Fig. 7.5. The calculated conditions are, $A_\Phi = 1.0\pi$, $\omega_m = 18.9$ KHz, and the ideal separation of a grating-lens pair is 150.2 mm, grating constant is 2000 lp/mm, and the gratings are aligned in Littrow configuration. And the grating separations are (a) 147.2 mm, (b) 148.7 mm, (c) 150.2 mm, (d) 151.7 mm, and (e) 153.2 mm, and the error ratios are (a) -2.0%, (b) -1.0 %, (c) 0.0 %, (d) +1.0%, and (e) +1.2%. By the calculation, the spatio-temporal coupling which is in proportion to the propagation time error is confirmed.

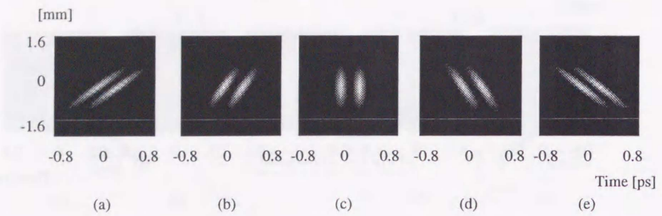

Figure 7.5: Spatio-temporal copuling induced by focal time error. The maginification M is 1.0, the amplitude, A_Φ, and frequency, ω_m, of the phase modulation, a time lens, are 1.0π rad and 18.9 Hz, respectively. The ideal separation of a grating-lens pair is 150.2 mm, grating constant is 2000 lp/mm, and the gratings are aligned in Littrow configuration. The errors are (a) -2%, (b) -1%, (c) 0%, (d) +1%, and (e) +2%, and the grating separations of each case are (a) 147.2 mm, (b) 148.7 mm, (c) 150.2 mm, (d) 151.7 mm, and (e) 153.2 mm

7.4.4 Spatio-Temporal Coupling Induced by Grating Angle Error

The grating angle error also induces spatio-temporal coupling. We calculat spatio-temporal output profiles with grating errors of G1 and G3 of Fig. 7.2. The parameters of the calculation are, $A_\Phi = 1.0\pi$, $\omega_m = 18.9$ KHz, and the separation of a grating pair is 150.2 mm, grating constant is 2000 lp/mm, the gratings are aligned in Littrow configuration, and the ideal incident angle of the grating G1 and G3 are 50.8 deg. The output profiles are shown if Fig. 7.6. The each grating angle error induces spatio-temporal coupling independently, and the direction of the coupling is depend on the direction of the angle error. In the case of the error of G1 and G2 is the same, the spatio-temporal coupling is disappered by counteract.

7.5 Summary

We have analyzed the spatio-temporal behavior of time microscope by using the spatio-temporal Wigner distribution function. The spatio-temporal coupling is induced by magnification changing, focal time error, propagation time error and grating angle error. The spatio-temporal profile of the ouptput pulse is very sensitive to these errors, even if the errors are less than few percents, the spatio-temporal copuling is critically large. However, the spatio-temporal coupling shall be counteractivelly reduced by combination of these spatio-temporla couplings.

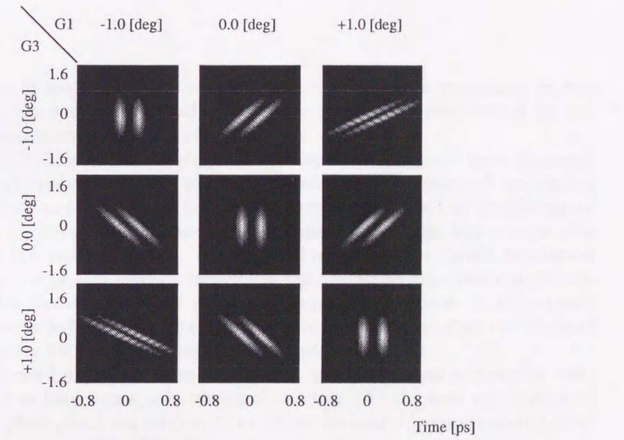

Figure 7.6: Spatio-temporal copuling induced by grating angle error. The maginification M is 1.0, the amplitude, A_Φ, and frequency, ω_m, of the phase modulation, a time lens, are 1.0π rad and 18.9 Hz, respectively. The separation of a grating-lens pair is 150 mm, grating constant is 2000 lp/mm, and the gratings are aligned in Littrow configuration. Angle-errors are induced on G1 and G3, in the range of -1.0 deg to +1.0 deg.

Chapter 8

Conclusions

The concept of spatio-temporal optical computing has been introduced in this thesis. In the chapter of introduction, we classified the concepts of spatio-temporal optical computing into three phases.

In the fist phase, by employing spatio-temporal duality, we have proposed a new signal analysis method which we name the phase-resolved correlation method. Most methods which have up to now been applied to interferogram analysis to improve the SNR can separate signals from noise, but are not able to separate independent signals. However, using the phase-resolved correlation method, we can clearly identify individual signals. In an experimental demonstration, the method shows its ability to identify a thickness of 18 μm and noise-masked interferogram signal peaks. We have confirmed that this method is very effective for analyzing low coherence interferograms.

In the second phase, we have employed a spatio-temporal conversion technique which is based on spatio-temporal analogy. As the first application of the second phase, we have proposed and demonstrated a spatio-temporal joint transform correlator (ST-JTC). The system based on similarity between a conventional spatial joint transform correlator, which is one of the most popular optical computing technique and a spectral filtering method, which is one of the most popular methods of controlling the temporal profile of an ultrafast light pulse. Our system is a hybrid of these two methods. In the demonstration, we determined the pulse separations of twin pulses which were synthesized by a Michelson interferometer. According to the result, we have confirmed that the experimental system has 12.4 fs temporal accuracy in determining the positions of input pulses.

As mentioned in the introduction, the ST-JTC is based on the idea of a spatial JTC. Almost all techniques of conventional JTC can be applied to the ST-JTC, such as nonlinear thresholding to increase the S/N ratio[27] or signal retrieval from rough phase noise[28]. Such unification of pulse control and conventional optical computing should yield a breakthrough in optical computing. Computational long distance communication and computational measurement should thus become possible.

As the second application of the second phase of the spatio-temporal optical computing, we have constructed a spectral interferometric three-dimensional surface-measurement system with only one-dimensional scanning operation and without the need for electronic computation.

The correlation which derived by the ST-JTC is not an intensity one but a complex correlation which includes information on the phase of the pulse. The ST-JTC does not depend on nonlinearity which depends on the high peak intensity of a pulse. This means that, we can use a super luminescent diode (SLD) or any other broad band light source as the input light source. With such light sources, the spatial output becomes the temporal coherence function of the input light source. Hence, we connected a conventional Michelson interferomter-based optical coherence tomography system and ST-JTC.

By the tomography system, we measured three samples to a depth-accuracy of 16 μm and depth-resolution of 70 μm. One is the path length difference of the Michelson interferometer, another is the surface of an aluminum coated sample and the last is the rough surface of a coin. Although the last sample is a highly light-scattering object, the system has demonstrated its ability to measure minute changes in the height of a sample surface.

In the third phase, we intended to apply spatio-temporal coupling into optical computing. As the first steps of the third phase spatio-temporal optical computing, we numerically investigate the spatio-temporal couplings in some diffractive optical components, a conventional pulse shaper, a spatio-temporal coupling pulse shaper, and a time-domain microscope. By employing the spatio-temporal Wigner distribution function, we reduced the amount of the numerical calculation of the spatio-temporal analysis.

In the first analysis, we numerically analyzed the spatio-temporal properties of several conventional pulse-shapers, specifically an ideal pulse-shaper, a pulse-shaper with lens defocus, with a grating-pair with different grating constant, with a lens-pair with different focal lengths and combinations of these using the Wigner distribution function.

In the case of lens defocus, we have confirmed that the spatio-temporal coupling effect induces a temporal chirp, and the velocity of the temporal frequency component is varied by the chirp. In the case with different grating constants, the degree of both the temporal and spatial frequency chirp is varied by combination of different grating constants, and the light pulse is moved on the spatial axis by the temporal chirp. In the case of different focal length lenses, the FWHM of the spatial profile is in proportion to focal length ratio, and the light pulse arrives at different place of the top and tail of the pulse induced by the temporal chirp. In the case with a different grating constant and focal length, the direction of the temporal and spatial frequency chirp is varied by the combination of the grating constant.

The quantization of the spatio-temporal coupling effect, as described above, suggests a number of practical applications which take advantage of the effects of specific temporal frequency on arbitrary spatial position which enable changes to be made to the beam direction of a light pulse. These applications will have potential for controlling the properties of high speed solid state components.

Next, we have proposed a spatio-temporally coupled pulse shaper (STCPS) for simultaneous spatial and temporal control of ultra fast light pulses by means of one-dimensional spatial light modulation. This system is the first endaevour to employ the spatio-temporal coupling. We have numerically analyzed the spatio-temporally coupled pulse shaper (STCPS) using the Wigner distribution function. Several behaviors of the STCPS were confirmed. Quadratic phase modulation by means of a lens causes the spatio-temporal pulse track to form a line whose inclination is in proportion to the focal length of the modulating lens.

Cubic phase modulation results in the spatio-temporal pulse track forming a curve of second degree whose second order coefficient is in proportion to the third order coefficient of the phase-mask. The influence of spatio-temporal coupling is controlled by the focal length ratio of coupling lenses to shaper lenses and the wavelength of the light source to the focal length of the shaper lens. x-ξ chirp occurs as a result of defocusing the coupling lens, although the x-t intensity profile on the output plane remains constant.

In the last analysis, we have analyzed the spatio-temporal behavior of time microscope by using the spatio-temporal Wigner distribution function. The spatio-temporal coupling is induced by magnification changing, focal time error, propagation time error and grating angle error. The spatio-temporal profile of the output pulse is very sensitive to these errors, even if the errors are less than few percents, the spatio-temporal coupling is critically large. However, the spatio-temporal coupling shall be counteractivelly reduced by combination of these spatio-temporal couplings.

In this thesis, we have introduced the concept of the spatio-temporal optical computing. We have confirmed that it is very effective to introduce conventional optical computing techiniques to time- and spatio-temporal domain employing spatio-temporal duality for improve the sensitivity and availability of optical measurement system. The concept is also effective to control ultrafast light pulse in higher dimmension.

The spatio-temporal optical computing will take more important place in the field of optical measurement and optical communication.

We have also investigated the applications of spatio-temporal optical computing techniques in the thesis. The main field of the application mentioned in this thesis is the field of optical measurement, however, the spatio-temporal optical computing techniques can be introduced into more wide field of optoelectronics, such as optical communications, optical memory or signal processing. The introduction shall extend the dimension of these fields into spatio-temporal domain, and achieve more intelligent and higher functional optoelectronics.

Appendix A

Program Sources

A.1 Phase-Resolved Correlation Method

The phase-resolved correlation method was implemented in Gnu Ocvtave and C-language. Although, the Gnu Octave version is the and an experimental prototype implementation, is more intuitively and methematically. The C version are written for Gnu Compiler Collection on Kondara MNU/Linux 1.2 and works with glibc 2.1.3 and FFTW library.

A.1.1 Gnu Octave implementation

Main Routine (prcm.m)

```
%%%%%%%%%%%%%%%%%%%%%%%%%%%%%%%%%%%%%%%%
%
% Analyze the correlation signal
%             of
%   White Lingt Interferometer
%             by
%  Phase Resolved Wavelet Transform
%
%   Written for Gnu Octave 2.0.16
%
%         Yoshiaki YASUNO
% <yasuno@optlab2.bk.tsukuba.ac.jp>
%           May 25th, 2000 -
%
%%%%%%%%%%%%%%%%%%%%%%%%%%%%%%%%%%%%%%%%

%%%%%%%%%% List of Variables %%%%%%%%%%
%
% ORIG : original correlation data.
% INP : correlation data without bias term.
% SPC : spectrum of INP.
% MW : mother wavelet
clear();
```

```
fig = 1;

%%% Read the data
load data.txt;     %% The data file is a \n-separated single column text.
ORIG = INP = data;

%%% The number of the data.
N = size(INP,1)

%%% Plot the original data.
figure(fig); fig = fig +1;
plot(INP);

%%% remove the bias form the original data
SPC = fft(INP);
RemovePoint = [1 2 3 N-1 N];
SPC(RemovePoint) = 0;
%INP = real(ifft(SPC));

%%% plot the spectrum of input data
figure(fig); fig = fig + 1;
plot(abs(SPC));

%%% find the maximun frequency
spc_max_value = max(SPC);
spc_max_point = 0;
for j = 1:size(SPC,1)
  if( SPC(j) == spc_max_value )
    spc_max_point = j
  endif
endfor


%%% calculate the correlation between
%%% the mother wavelet and input signel
fig ++; fig_phase = fig;
fig ++; fig_mother = fig;

%%% the frequency and wavelength of mother wavelet
mw_f = (spc_max_point -1 ) / N;
%mw_f = (spc_max_point -2 ) / N;
mw_wavelength = 1 / mw_f;

%%% make X axis
for j = 1:N
  %% 0.85 means 0.85 um, the %%wavelength of light source
  realwavelength = 0.85;
  X(j) = j * mw_f * realwavelength;
endfor
```



```
X = X - max(X)/2;

phase_resolution = 32;
phase_range = 1.6 * pi;
phase_bias = 1.6 * pi;
for k = 1:phase_resolution;
  mw_phase = (k-1)/phase_resolution * phase_range - phase_bias;
  mw_shift = 0;
  for j = 1:N
    %%% Generate the Motherwavelet
    mw_shift = j - 1 ;
    mw_envelope = shift(gauss( (1:N)'-N/2, 0.2*N), mw_shift  + N/2 );
    MW =  sin(mw_f * 2 * pi .* (1:N)' + mw_phase) .* mw_envelope;
    PRWLT(k,j) = sum( MW .* INP );
  endfor
  %%% make Y axis for plotting the results
  Y(k) = (mw_phase + phase_bias)/pi;
  k
endfor

TMP = PRWLT;
TMP = TMP + min(min(TMP));
TMP = TMP ./ max(max(TMP));
TMP = TMP * 128;
colormap(gray(128));

figure (fig); fig ++;
gset contour surface
figure (fig); fig ++;
gset nogrid
gset xlabel 'Position [um]'
gset ylabel 'Phase [prad]'
gset size 1,1
contour (rot90(rot90(rot90((PRWLT)))) , 30, X, Y);
%% print out the contour plot in tgif file

gset terminal tgif
gset output 'contour.obj'
gset size 0.57,0.57
replot
gset output
gset terminal X

figure(1)
plot(X, INP ./ max(INP));
gset nogrid
gset size 0.57,0.57
gset terminal tgif
gset output 'inputsignal.obj'
gset ylabel 'Intensity [a.u.]'
```

```
replot
gset output
gset terminal X

figure(2)
mw_envelope = gauss( (1:N)'-N/2, 0.03*N);
MW = sin(mw_f * 2 * pi .* (1:N)') .* mw_envelope;
plot(X, MW ./ max(MW));
gset nogrid
gset size 0.57,0.57
gset terminal tgif
gset output 'mother.obj'
gset ylabel 'Intensity [a.u.]'
replot
gset output
gset terminal X

save prwlt.octave PRWLT;
```

Gaussian Function (gauss.m)

```
%%%%%%%%%%%%%%%%%%%%%%%%%%%%%%%%%%%%%%%%%%%%%%%%%%%%%%%%%%%%%%%%%%%%%%%%%%%%
% Gaussian Function
%%%%%%%%%%%%%%%%%%%%%%%%%%%%%%%%%%%%%%%%%%%%%%%%%%%%%%%%%%%%%%%%%%%%%%%%%%%%
%
% t: Time
% b: Dispersion
function result = gauss(t,b)
  result = exp(-pi*(t/b).^2);
endfunction
```

A.1.2 C Language Implementation

```
/*************************************************
 Phase-Resolved Corerlation Algorithm
    Version 1.00.c

     Programed by Yoshiaki Yasuno
  <yasuno@optlab2.bk.tsukuba.ac.jp>
      Written for GCC Ver. 2.95
 of Linux 2.2.17pre14, Kondara/MNU Linux 2.0
              with FFTW
   Sep. 26th, 2000

$Id: c_program.tex,v 1.3 2001/01/24 03:52:29 yasuno Exp $

*************************************************/

#include <stdio.h>
#include <math.h>
```



```
#include <string.h>
#include <fftw.h>

/* Definition of Scientific Constants */
#define Pi 3.141592

/* The fdouble must be double or float. */
typedef double fdouble;

/* If you would not to use these features,
   do not define these macros. */
#define INLINE inline
#define REGISTER register

/* Prototypes of Function */
int read_data_from_file (char *input_file_name,
                         int number_of_data, fdouble *interferogram);
int get_number_of_data (char *input_file_name);
int search_spectrum_peak (int number_of_data, fdouble *interferogram);
INLINE fdouble *make_envelope_array (fdouble width, int number_of_data,
                                     fdouble *envelope, int shift_value);
fdouble *make_carrer_array (int spectrum_peak_position, fdouble phase_bias,
   int number_of_data, fdouble *carrer);
INLINE fdouble gauss(fdouble width, fdouble x);
INLINE fdouble *shift (int number_of_data, fdouble *array, int shift_value);
INLINE fdouble *mult_arry_elements(fdouble *result, fdouble *operand1,
                                   fdouble *operand2, int number_of_data);
INLINE fdouble *mult_three_arry_elements(fdouble *result, fdouble *operand1,
                                         fdouble *operand2, fdouble *operand3,
                                         int number_of_data);
INLINE int prc_coordinates (int phase, int shift, int number_of_data);
INLINE fdouble sigma_array(fdouble *array, int number_of_data);

/***************************************
 * Start of main function
 ***************************************/
/* The arguments have no sence yet. */
int main (int argc, char *argv[])
{
  /***************************************
   * Decralation of Variables
   ***************************************/
  /* The text file name, which contains the interferogram data
     in the format of TABed or CRed data array. */
  char *input_file_name = argv[1];
  /* The size of array data. */
  const int number_of_data = get_number_of_data(input_file_name);
  /* Data arrays for original interferogram,
     carrier sinusoidal wave, the envelope of mother wavelet and
     interferogram .* motherwavelet. */
```

```
fdouble *interferogram = calloc(sizeof(fdouble), number_of_data);
fdouble *carrer = calloc(sizeof(fdouble), number_of_data);
fdouble *envelope = calloc(sizeof(fdouble), number_of_data);
fdouble *correlated_interferogram
          = calloc(sizeof(fdouble), number_of_data);
/* Width of the mother wave let, that is
   the coefficient of Gaussian function */
fdouble width = 0.07 * number_of_data;
/* Analysing phase range and its bias.
   The analysis is started from phase_range_bias. */
fdouble phase_range = 1.6 * Pi;
fdouble phase_range_bias = 1.6 * Pi;
/* Pahse_variable for calculation of mother wavelet. */
fdouble phase_bias = 0.0;
/* The number of Sampling points in phase axis */
int phase_resolution = 256;
/* Result matrix in Phase-Shift(Position) plane:
   Phase-Resolved Correlation */
fdouble *prc = calloc(sizeof(fdouble),
                      number_of_data * phase_resolution);
/* Variable of iteration index */
int spectrum_peak_position;
int mother_shift;
int mother_shift_period = 5;
int i;
int status;

/***************************************
 * The start of PRCM process
 ***************************************/
/* Read the data form file */
status = read_data_from_file (input_file_name,
                              number_of_data, interferogram);
if ( status != 0 )
  {
    fprintf (stderr, "Usage: %s filename\n", argv[0]);
    exit (1);
  }
/* Seach the position of the spectrum peak
    which is the carrier frequency */
spectrum_peak_position
    = search_spectrum_peak (number_of_data, interferogram);
/* Shift the original interferogram to adjust
   the position of the result, PRC to make it much visible. */
shift( number_of_data, interferogram, number_of_data/2);

/************************************************************
 * The start of Phase-Resolved Correlation Algorhysm
 ************************************************************/
/* The outer loop is for scanning on phase axis. */
```



```
  for ( i=0; i<phase_resolution ; i++)
    {
      phase_bias = phase_range / phase_resolution
                               * (fdouble)i - phase_range_bias;
      make_carrer_array (spectrum_peak_position,
                         phase_bias, number_of_data, carrer);
      for (mother_shift=0; mother_shift<number_of_data;
           mother_shift += mother_shift_period)
{
  make_envelope_array (width, number_of_data, envelope, mother_shift);
  mult_three_arry_elements(correlated_interferogram, envelope, carrer,
   interferogram, number_of_data);
  prc[ prc_coordinates (i, mother_shift, number_of_data) ]
  = sigma_array(correlated_interferogram, number_of_data);
}
    }


  fprintf(stderr,"The max position of the spectrum is %d.\n",
          spectrum_peak_position);

  for ( i=0; i<phase_resolution ; i++)
    {
      for (mother_shift=0; mother_shift<number_of_data;
           mother_shift += mother_shift_period)
{
  printf ("%f", prc[ prc_coordinates (i, mother_shift, number_of_data) ]);
  printf ((mother_shift != number_of_data-1)?" ":"");
}
      printf ("\n");
    }

  exit (0);
}

/***************************************
 * Multiplication of each element of array
 ***************************************/
INLINE fdouble *mult_arry_elements(fdouble *result, fdouble *operand1,
                                   fdouble *operand2, int number_of_data)
{
  int i;
  for (i=0; i<number_of_data; i++)
    result[i] = operand1[i] * operand2[i];

  return(result);
}

/***************************************
 * Multiplication of each element of three arrays
```

```
 ***************************************/
INLINE fdouble *mult_three_arry_elements(fdouble *result,
                                         fdouble *operand1,
                                         fdouble *operand2,
                                         fdouble *operand3,
                                         int number_of_data)
{
  REGISTER int i;
  for (i=0; i<number_of_data; i++)
    result[i] = operand1[i] * operand2[i] * operand3[i];

  return(result);
}

INLINE int prc_coordinates (int phase, int shift, int number_of_data)
{
  return (phase * number_of_data + shift);
}
/***************************************
 * Read the 1-D data from text file
 ***************************************/
/* This function overwrite the 1-D array interferogram,
   and returns the pointer which points the array, interferogram. */
int read_data_from_file (char *input_file_name, int number_of_data,
                         fdouble *interferogram)
{
  float tmp_float;
  int i;
  FILE *ifp; /* Input file pointer */

  ifp = fopen(input_file_name,"r");

  if ( ifp == NULL ){
    fprintf (stderr, "Can not open the file; %s.\n", input_file_name);
    exit (1);
  }

  for ( i=0; i<1100 ; i++)
    {
      fscanf (ifp, "%e", &tmp_float);
      interferogram[i] = (fdouble)tmp_float;
    }
  fclose(ifp);

  return (0);
}

int get_number_of_data (char *input_file_name){
  int number_of_data = 1;
  float null;
```



```
  FILE *ifp; /* Input file pointer */

  ifp = fopen(input_file_name,"r");

  if ( ifp == NULL ){
    fprintf (stderr, "Can not open the file; %s.\n", input_file_name);
    exit (1);
  }

  while ( fscanf (ifp, "%e", &null) != EOF ){
    /* fprintf (stderr,"%d: %f\n", i, tmp_float); */
    number_of_data ++;
  }
  number_of_data --;
  return (number_of_data);
}
/***************************************
 * Find the peak position of the spectrum
 ***************************************/
/* This function returns the postion of the peak */
/* The function demands FFTW library.
   http://www.fftw.org/                  */
int search_spectrum_peak (int number_of_data, fdouble *interferogram)
{
  int i;
  fdouble max_value = 0.0;
  fdouble power;
  int max_point = 0;

  fftw_complex in[number_of_data], out[number_of_data];
  fftw_plan plan;

  for ( i=0; i<number_of_data; i++)
    {
      c_re(in[i]) = interferogram[i];
      c_im(in[i]) = 0.0;
    }

  plan = fftw_create_plan (number_of_data, FFTW_FORWARD, FFTW_ESTIMATE);
  fftw_one (plan, in, out);
  fftw_destroy_plan (plan);


  for ( i=2; i<number_of_data/2; i++)
    {
      power =  c_re(out[i])*c_re(out[i])+c_im(out[i])*c_im(out[i]);
      if ( power > max_value ){
max_point = i;
max_value = power;
      }
```

```
    }

  return (max_point);
}

INLINE fdouble fftwy_power(fftw_complex ftc)
{
  return( c_re(ftc)*c_re(ftc)+c_im(ftc)*c_im(ftc));
}

/*************************************
 * Make carrer frequency array
 *************************************/
fdouble *make_carrer_array (int spectrum_peak_position,
                            fdouble phase_bias,
    int number_of_data,
                            fdouble *carrer)
{
  int i;
  fdouble frequency = (fdouble)spectrum_peak_position
                    / (fdouble)number_of_data;
  fdouble x;
  /* MW = sin(mw_f * 2 * pi .* (1:N)' + mw_phase) .* mw_envelope; */

  for (i=0; i<number_of_data; i++)
    {
      x = (fdouble)i;
      carrer[i] = sin (frequency * 2.0 * Pi * x + phase_bias);
    }
  return (carrer);
}

/*************************************
 * Make Gaussian envelope
 *************************************/
INLINE fdouble *make_envelope_array (fdouble width,
                                     int number_of_data,
                                     fdouble *envelope,
                                     int shift_value)
{
  REGISTER int i;
  fdouble x;
  REGISTER fdouble n_of_data_devided_by_2 = (fdouble)number_of_data/2.0;

  for ( i=0; i<number_of_data; i++)
    {
      x = (fdouble)i - n_of_data_devided_by_2;
      envelope[i] = gauss(width, x);
      /*      fprintf(stdout,"%e\n",envelope[i]); */
    }
```



```
  shift(number_of_data, envelope, shift_value);
  return(envelope);
  /*   mw_envelope = shift(gauss( (1:N)'-N/2, 0.2*N), mw_shift  + N/2 ); */
}

INLINE fdouble gauss(fdouble width, fdouble x){
  fdouble x_devided_by_width = x/width;
  return ( exp(-Pi*(x_devided_by_width)*(x_devided_by_width)) );
}

INLINE fdouble *shift (int number_of_data, fdouble *array, int shift_value)
{
  REGISTER int i;
  int shift_position;
  fdouble *result_array = calloc (sizeof(fdouble), number_of_data);
#ifdef SAFETY
  while( shift_value > number_of_data )
    shift_value -= number_of_data;

  while( shift_value < 0 )
    shift_value += number_of_data;
#endif

  for ( i=0; i<number_of_data; i++)
    {
      shift_position = i+shift_value;
      result_array[i] = array[
      (shift_position < number_of_data)
      ? shift_position
      : shift_position-number_of_data ];
    }

  memcpy(array, result_array, sizeof(fdouble)*number_of_data);
  free (result_array);

  return (array);
}


INLINE fdouble sigma_array(fdouble *array, int number_of_data)
{
  REGISTER int i;
  fdouble sum = 0.0;

  for (i=0; i<number_of_data; i++)
    sum += array[i];

  return (sum);
}
```

A.2 Wigner Analysis

A.2.1 Makefile

```
#
# Makefile for Numerical Analysis of Time Domain Microscope
#
# Programmed by Yoshiaki Yasuno
# <yasuno@optlab2.bk.tsuukba.ac.jp>
#
OPT=-O7
CFLAGS=-Wall

wigner : main.o calc_results.o
g++ ${OPT} -o $@ main.o calc_results.o
main.o : main.cpp parameters.h coordinate_transform.h WinST.h CtoA.h
g++ ${OPT} $(CFlAGS) -c main.cpp
calc_results.o : calc_results.cpp CtoA.h Ns.h parameters.h
g++ ${OPT} $(CFlAGS) -c calc_results.cpp
```

A.2.2 main.cpp

```
/*******************************************
  Wigner Distribution Function による
  光パルスの時空間解析

  Oct. 19th, 1999-

  Yoshiaki YASUNO
  yasuno@optlab2.bk.tsukuba.ac.jp
*******************************************/

#include<iostream.h>
#include<fstream.h>
#include<math.h>

#include"parameters.h"
#include"coordinate_transform.h"
#include"WinST.h"
#include"CtoA.h"
#include"calc_results.h"
#include"Ns.h"

/*************************************
 * Start of the main function
 *************************************/
int main (void){
  int i_x, i_xi, i_t, i_om; // loop-index of x, xi, t and omega.
  Ns N (NX,NXI,NT,NOM); // Structure Ns, which contains the size of a
                        // result 4-D matrix.
```



```
  /*****************************
   * Print out the parameters
   * (for debug)
   *****************************/
  cout << "alpha = " << alpha << "\n";
  cout << "beta = " << beta << "\n";
  cout << "alpha1 = " << alpha1 << "\n";
  cout << "beta1 = " << beta1 << "\n";
  cout << "zt1bb = " << zt1 * (beta * beta) << "\n";
  cout << "zt2bb = " << zt2 * (beta * beta) << "\n";
  cout << "ft = " << ft << "\n";
  cout << "mom = " << mom << "\n";
  cout << "theta = " << theta << "\n";
  cout << "k = " << k << "\n";

  /*************************************
   * Calculate the Spatio-Temporal
   * Winger Distribution Function
   *************************************/
  float *Wst; // Result matrix
  Wst = new float[N.total_size()];

  for( i_x=0 ; i_x < NX ; i_x++){
    for( i_xi=0 ; i_xi < NXI ; i_xi++){
      for( i_t=0 ; i_t < NT ; i_t++){
for( i_om=0 ; i_om < NOM ; i_om++){
  coordinate xt( (double(i_x)  - double(NX/2))*dx,
 (double(i_xi) - double(NXI/2))*dxi,
 (double(i_t)  - double(NT/2))*dt,
 (double(i_om) - double(NOM/2))*dom
);
  /*
   * Coordinate transform routines.
   * Select on of them.
   */
  //xt = TImaging (xt, alpha1, beta1, k, zt1, zt2, pw2);
  xt = TImagingVG (xt, alpha1, beta1, alpha2, beta2,
   alpha3, beta3, alpha4, beta4, k, zt1, zt2, pw2);
  //xt = TImagingUnion (xt, beta, k, pw2, ztm);
  //xt = TImagingFT (xt, alpha, beta, k, zt1, zt2, pw2, ftf);
  //xt = TImagingPropagation (xt, alpha, beta, k, zt1, zt2, pw2, az);
  //xt = TImagingDefocus2 (xt, alpha, beta,
  //   k, zt1, zt2, pw2, alpha_defocus);

  Wst[N.CtoA(i_x,i_xi,i_t,i_om)] = WinSTdouble( xt );
}
      }
    }
    cerr << i_x+1 << "/" << NX << " done.\n";
```

```
  }

  /************************************************
   * Calculate and output the result electric
   * field distributions to files.
   ************************************************/
  calc_ixit(Wst, N);
  calc_ixt(Wst, N);
  calc_ixxi(Wst, N);
  calc_iomx(Wst, N);
  calc_iomt(Wst, N);
  calc_iomxi(Wst, N);
  calc_ix(Wst, N);
  calc_ixi(Wst, N);
  calc_it(Wst, N);
  calc_iom(Wst, N);

  delete[] Wst;

  exit (0);
}
```

A.2.3 calc_results.h

```
/*************************************
 * Prototypes for calc_results.cpp
 *************************************/
#ifndef __calc_results_h__
#define __calc_results_h__

#include"Ns.h"
void calc_ixit(float *Wst, Ns N);
void calc_ixt(float *Wst, Ns N);
void calc_ixxi(float *Wst, Ns N);
void calc_iomx(float *Wst, Ns N);
void calc_iomt(float *Wst, Ns N);
void calc_iomxi(float *Wst, Ns N);

void calc_ix (float *Wst, Ns N);
void calc_ixi (float *Wst, Ns N);
void calc_it(float *Wst, Ns N);
void calc_iom (float *Wst, Ns N);

#endif // __calc_results_h__
```

A.2.4 calc_results.cpp

```
#include <fstream.h>
#include <math.h>
#include "CtoA.h"
```



```
#include "Ns.h"
#include "parameters.h"

/*****************************
 * |E(xi,t)|^2
 *****************************/
void calc_ixit (float *Wst, Ns N)
{
  int i_x, i_xi, i_t, i_om;

  // Initialize result matrix
  float Exit2[N.XI][N.T];
  for( i_xi=0 ; i_xi<N.XI ; i_xi++)
    for( i_t=0 ; i_t<N.T ; i_t++)
      Exit2[i_xi][i_t] = 0.0;

  for( i_x=0 ; i_x<N.X ; i_x++)
    for( i_xi=0 ; i_xi<N.XI ; i_xi++)
      for( i_t=0 ; i_t<N.T ; i_t++)
for( i_om=0 ; i_om<N.OM ; i_om++)
  Exit2[i_xi][i_t] += Wst[N.CtoA(i_x,i_xi,i_t,i_om)];

  // File output
  ofstream Ixit("Ixit.mtx");
  for( i_xi=0 ; i_xi<N.XI ; i_xi++)
    for( i_t=0 ; i_t<N.T ; i_t++){
      Ixit << Exit2[i_xi][i_t];
      if( i_t != N.T-1 ){ Ixit <<"\t"; }else{ Ixit<<"\n"; }
    }
  Ixit.close();
}

/*****************************
 * |E(x,t)|^2
 *****************************/
void calc_ixt (float *Wst, Ns N)
{
  int i_x, i_xi, i_t, i_om;

  // Initialize result matrix
  float Ext2[N.X][N.T];
  for( i_x=0 ; i_x<N.X ; i_x++)
    for( i_t=0 ; i_t<N.T ; i_t++)
      Ext2[i_x][i_t] = 0.0;

  for( i_x=0 ; i_x<N.X ; i_x++)
    for( i_t=0 ; i_t<N.T ; i_t++)
      for( i_xi=0 ; i_xi<N.XI ; i_xi++)
for( i_om=0 ; i_om<N.OM ; i_om++)
  Ext2[i_x][i_t] += Wst[N.CtoA(i_x,i_xi,i_t,i_om)];
```

```
  // File output
  ofstream Ixt("Ixt.mtx");
  for( i_x=0 ; i_x<N.X ; i_x++)
    for( i_t=0 ; i_t<N.T ; i_t++){
      Ixt << Ext2[i_x][i_t];
      if( i_t != N.T-1 ){ Ixt <<"\t"; }else{ Ixt<<"\n"; }
    }

  Ixt.close();
}

/*****************************
 * |E(x,xi)|^2
 *****************************/
void calc_ixxi (float *Wst, Ns N)
{
  int i_x, i_xi, i_t, i_om;
  float Exxi2[N.X][N.XI];
  // Initialization of Exxi2
  for( i_x=0 ; i_x<N.X ; i_x++)
    for( i_xi=0 ; i_xi<N.XI ; i_xi++)
      Exxi2[i_x][i_xi] = 0.0;

  // Integration along t and omega
  for( i_x=0 ; i_x<N.X ; i_x++)
    for( i_xi=0 ; i_xi<N.XI ; i_xi++)
      for( i_t=0 ; i_t<N.T ; i_t++)
for( i_om=0 ; i_om<N.OM ; i_om++)
  Exxi2[i_x][i_xi] += Wst[N.CtoA(i_x,i_xi,i_t,i_om)];

  // file output
  ofstream Ixxi("Ixxi.mtx");
  for( i_x=0 ; i_x<N.X ; i_x++)
    for( i_xi=0 ; i_xi<N.XI ; i_xi++){
      Ixxi << Exxi2[i_x][i_xi];
      if( i_xi != N.XI-1 ){ Ixxi <<"\t"; }else{ Ixxi<<"\n"; }
    }
  Ixxi.close();
}

/*****************************
 * |E(x,om)|^2
 *****************************/
void calc_iomx (float *Wst, Ns N)
{
  int i_x, i_xi, i_t, i_om;
  float Eomx2[N.OM][N.X];
  // Initialization of Exom2
  for( i_om=0 ; i_om<N.OM ; i_om++)
```



```
    for( i_x=0 ; i_x<N.X ; i_x++)
      Eomx2[i_om][i_x] = 0.0;

  // Integration
  for( i_om=0 ; i_om<N.OM ; i_om++)
    for( i_x=0 ; i_x<N.X ; i_x++){
      for( i_xi=0 ; i_xi<N.XI ; i_xi++){
for( i_t=0 ; i_t<N.T ; i_t++)
  Eomx2[i_om][i_x] += Wst[N.CtoA(i_x,i_xi,i_t,i_om)];
      }
      Eomx2[i_om][i_x] *= (1.0/2.0*Pi);
    }

  // file output
  ofstream Iomx("Iomx.mtx");
  for( i_om=0 ; i_om<N.OM ; i_om++)
    for( i_x=0 ; i_x<N.X ; i_x++){
      Iomx << Eomx2[i_om][i_x];
      if( i_x != N.X-1 ){ Iomx <<"\t"; }else{ Iomx<<"\n"; }
    }
  Iomx.close();
}

/*****************************
 * |E(t,om)|^2
 *****************************/
void calc_iomt (float *Wst, Ns N)
{
  int i_x, i_xi, i_t, i_om;
  float Eomt2[N.OM][N.T];

  // Initialazation of Etom2
  for( i_om=0 ; i_om<N.OM ; i_om++){
    for( i_t=0 ; i_t<N.T ; i_t++){
      Eomt2[i_om][i_t] = 0.0;
    }
  }

  // Integration
  for( i_x=0 ; i_x<N.X ; i_x++)
    for( i_xi=0 ; i_xi<N.XI ; i_xi++)
      for( i_om=0 ; i_om<N.OM ; i_om++)
for( i_t=0 ; i_t<N.T ; i_t++)
  Eomt2[i_om][i_t] += Wst[N.CtoA(i_x,i_xi,i_t,i_om)];

  ofstream Iomt("Iomt.mtx");
  for( i_om=0 ; i_om<N.OM ; i_om++)
    for( i_t=0 ; i_t<N.T ; i_t++ ){
      Iomt << Eomt2[i_om][i_t];
      if( i_t != N.T-1 ){ Iomt <<"\t"; }else{ Iomt<<"\n"; }
```

```
    }
  Iomt.close();
}

/*****************************
 * |E(om,xi)|^2
 *****************************/
void calc_iomxi (float *Wst, Ns N)
{
  int i_x, i_xi, i_t, i_om;
  float Eomxi2[N.OM][N.XI];

  // Initialazation of Etom2
  for( i_om=0 ; i_om<N.OM ; i_om++){
    for( i_xi=0 ; i_xi<N.XI ; i_xi++){
      Eomxi2[i_om][i_xi] = 0.0;
    }
  }

  // Integration
  for( i_x=0 ; i_x<N.X ; i_x++)
    for( i_xi=0 ; i_xi<N.XI ; i_xi++)
      for( i_t=0 ; i_t<N.T ; i_t++)
for( i_om=0 ; i_om<N.OM ; i_om++)
  Eomxi2[i_om][i_xi] += Wst[N.CtoA(i_x,i_xi,i_t,i_om)];

  ofstream Iomxi("Iomxi.mtx");
  for( i_om=0 ; i_om<N.OM ; i_om++)
    for( i_xi=0 ; i_xi<N.XI ; i_xi++ ){
      Iomxi << Eomxi2[i_om][i_xi];
      if( i_xi != N.XI-1 ){ Iomxi << "\t"; }else{ Iomxi << "\n"; }
    }
  Iomxi.close();
}

/*****************************
 * |E(x)|^2
 *****************************/
void calc_ix (float *Wst, Ns N)
{
  int i_x, i_xi, i_t, i_om;
  float Ex2[N.X];

  // Initialazation of Eit2
  for( i_x=0 ; i_x<N.X ; i_x++)
    Ex2[i_x] = 0.0;

  // Integration
  for( i_x=0 ; i_x<N.X ; i_x++)
    for( i_xi=0 ; i_xi<N.XI ; i_xi++)
```



```
      for( i_t=0 ; i_t<N.T ; i_t++)
for( i_om=0 ; i_om<N.OM ; i_om++)
  Ex2[i_x] += Wst[N.CtoA(i_x,i_xi,i_t,i_om)];

  ofstream Ix("Ix.mtx");
  for( i_x=0 ; i_x<N.X ; i_x++ )
    Ix << Ex2[i_x] << "\n";
   Ix.close();
}

/*****************************
 * |E(xi)|^2
 *****************************/
void calc_ixi (float *Wst, Ns N)
{
  int i_x, i_xi, i_t, i_om;
  float Exi2[N.XI];

  // Initialazation of Eit2
  for( i_xi=0 ; i_xi<N.XI ; i_xi++)
    Exi2[i_xi] = 0.0;

  // Integration
  for( i_x=0 ; i_x<N.X ; i_x++)
    for( i_xi=0 ; i_xi<N.XI ; i_xi++)
      for( i_t=0 ; i_t<N.T ; i_t++)
for( i_om=0 ; i_om<N.OM ; i_om++)
  Exi2[i_xi] += Wst[N.CtoA(i_x,i_xi,i_t,i_om)];

  ofstream Ixi("Ixi.mtx");
  for( i_xi=0 ; i_xi<N.XI ; i_xi++ )
    Ixi << Exi2[i_xi] << "\n";
   Ixi.close();
}

/*****************************
 * |E(t)|^2
 *****************************/
void calc_it (float *Wst, Ns N)
{
  int i_x, i_xi, i_t, i_om;
  float Et2[N.T];

  // Initialazation of Eit2
  for( i_t=0 ; i_t<N.T ; i_t++)
    Et2[i_t] = 0.0;

  // Integration
  for( i_x=0 ; i_x<N.X ; i_x++)
    for( i_xi=0 ; i_xi<N.XI ; i_xi++)
```

```
      for( i_t=0 ; i_t<N.T ; i_t++)
for( i_om=0 ; i_om<N.OM ; i_om++)
  Et2[i_t] += Wst[N.CtoA(i_x,i_xi,i_t,i_om)];

  ofstream It("It.mtx");
  for( i_t=0 ; i_t<N.T ; i_t++ )
    It << Et2[i_t] << "\n";
   It.close();
}

/*****************************
 * |E(om)|^2
 *****************************/
void calc_iom (float *Wst, Ns N)
{
  int i_x, i_xi, i_t, i_om;
  float Eom2[N.OM];

  // Initialazation of Eit2
  for( i_om=0 ; i_om<N.OM ; i_om++)
    Eom2[i_om] = 0.0;

  // Integration
  for( i_x=0 ; i_x<N.X ; i_x++)
    for( i_xi=0 ; i_xi<N.XI ; i_xi++)
      for( i_t=0 ; i_t<N.T ; i_t++)
for( i_om=0 ; i_om<N.OM ; i_om++)
  Eom2[i_om] += Wst[N.CtoA(i_x,i_xi,i_t,i_om)];

  ofstream Iom("Iom.mtx");
  for( i_om=0 ; i_om<N.OM ; i_om++ )
    Iom << Eom2[i_om] << "\n";
   Iom.close();
}
```

A.2.5 parameters.h

```
#
# parameters.h
#
# In this file, we define the parameters
# of the numerical analysis

#include <math.h>
const double Pi = asin(1.0)*2.0;
const double C = 3e8;

/*************************************
 * Parameters which you can change.
 *************************************/
```



```
const double lambda = 775e-9; // Wavelength [m]
const int NX     = 32;
const int NXI    = 32;
const int NTM    = 1;
const int NT     = 32*NTM;
const int NOM    = 32;
const double wx  = 2.0e-3;        // FWHM of x = 2[mm] for sinusoidal
const double wt  = 100.0e-15;     // FWHM of y = 100[fs]
const double dx  = 0.1e-3;      // Sampling period of x = 0.1[mm]
const double dxi = Pi/(double(NXI)*0.1e-3); // Sampling period of xi[rad/m]
const double dt  = 50.0e-15;      // Sampling period of t[s]
const double dom = 2.0*Pi/(double(NOM)*dt) ; // Sampling period of omega[rad/s]

const double alpha = 1.0; // Parameter of grating
const double f = 60e-3; // focus length of lens[m]
const double k = 8.3841e6; // wave vector[rad/m]
const double d = 1.0e-3/2000.0;
const double theta = asin(lambda/(2*d));
const double beta = 2.0*Pi/(d*cos(theta)*(2*Pi*C/lambda));
const double f_d = 130e-3; // focal length of incident lens
const double defocus1 = 0.8;
const double defocus2 = 1.0;
const double apl = 00e-3;  //Length of after propergation
const double cv = 500*Pi/(2e-2*2e-2) * -0.7 * 5; // curve of square
const double ff=700e-3; // focal length of pahse filter lens of devia
const double shift = 0.0;

/*************************************
 * calculated alpha and beta
 *************************************/
#define diford 1.0 // diffraction order
const double thetai1 = 51.805 / 360.0 * 2 * Pi; /* incident angle [rad] */
const double thetad1 = asin( diford * lambda / d - sin( thetai1) );
const double alpha1 = cos(thetai1) / cos(thetad1);
const double beta1 = lambda * diford / (d * C * cos(thetad1));
#undef diford

#define diford 1.0 // diffraction order
const double thetai2 = 50.805 / 360.0 * 2 * Pi; /* incident angle [rad] */
const double thetad2 = asin( diford * lambda / d - sin( thetai2) );
const double alpha2 = cos(thetai2) / cos(thetad2);
const double beta2 = lambda * diford / (d * C * cos(thetad2));
#undef diford

#define diford 1.0 // diffraction order
const double thetai3 = 51.805 / 360.0 * 2 * Pi; /* incident angle [rad] */
const double thetad3 = asin( diford * lambda / d - sin( thetai3) );
const double alpha3 = cos(thetai3) / cos(thetad3);
const double beta3 = lambda * diford / (d * C * cos(thetad3));
#undef diford
```

```
#define diford 1.0 // diffraction order
const double thetai4 = 50.805 / 360.0 * 2 * Pi; /* incident angle [rad] */
const double thetad4 = asin( diford * lambda / d - sin( thetai4) );
const double alpha4 = cos(thetai4) / cos(thetad4);
const double beta4 = lambda * diford / (d * C * cos(thetad4));
#undef diford

/***************************************
 * Temporal Imaging System
 ***************************************/
const double mpm = Pi * 1.0;       // Amplitude of the phase modulation
const double mom = 3.0e3 * 2.0 * Pi;  // Frequency of the phase modulation
const double ft = k / (mpm * mom * mom);
const double ztm = 1.00; // Magnitude of Time Microscope
const double zt1 = (alpha2 * alpha2)
  / (beta2 * beta2) * ft * ( 1.0 + (1.0 / ztm) );
const double zt2 = (alpha4 * alpha4) / (beta4 * beta4) * ft * ( 1.0 + ztm );
const double pw2 = k / ft * 1.00;
const double az = 100.0e-3; // Propagation after imaging [m]
const double ftf = 000.0e-3; // Last FT lens
const double alpha_defocus = -0.00;


/***************************************
 * Temporal 2-f Imaging
 ***************************************/
const double ft1 = ft;
const double ft2 = ft;
const double pw2_1 = k / ft1;
const double pw2_2 = k / ft2;

/***************************************************
 * Don't change the parameters.
 * They are calculated by the above parameters.
 ***************************************************/
const double a = 1.0/2.0*sqrt(2.0/log(2.0))*wx;
const double b = 1.0/2.0*sqrt(2.0/log(2.0))*wt;
const double w_bias = a*b/(2.0*Pi);
const double w_x = -(2.0/(a*a));
const double w_xi = -(a*a/2.0);
const double w_t = -(2.0/(b*b));
const double w_om = -(b*b/2.0);
```

A.2.6 coordinate_transform.h

```
/*****************************************************
  The definition of class for 4 valuables coordinate
                class coordinate
                      and
```



```
 Functions for coordinate transform
 *****************************************************/

/***************************************
 * Definition of class coordinate
 ***************************************/
#include<math.h>
class coordinate{
public:
  double x, xi, t, om;
  inline coordinate(){
    set(0.0, 0.0, 0.0, 0.0);
  }
  inline coordinate(double x, double xi, double t, double om){
    set(x, xi, t, om);
  }
  inline void set(double x, double xi, double t, double om){
    this->x = x;
    this->xi = xi;
    this->t = t;
    this->om = om;
  }
};

/*************************************************
 * Functions for coordinate transform
 *************************************************/

/*
 * Do nothing
 */
inline coordinate Vacuum(coordinate org){
  return(org);
}

/*
 * Spatial Lens
 */
inline coordinate SpatialLens(coordinate org, double f, double k){
  return( coordinate( org.x,
      k/f * org.x + org.xi,
      org.t,
      org.om ) );
}

/*
 * Propagation in Dispersion Medium
 */
inline coordinate Propagation(coordinate org, // The original coordinate
      double z,       // Propagation Distance
```

```
      double k,       // Transversive Wave Vector
      double gd)      // Group Delay (d^2k/kom^2)
{
  return( coordinate( org.x - z/k *org.xi,
      org.xi,
      org.t - gd*z*org.om,
      org.om ));
}

/*
 * Input Grating
 */
inline coordinate GratingIn(coordinate org, // The original coordinate
    double alpha,   // Parameter of Grating
    double beta)    // Parameter of Grating
{
  return( coordinate( double(alpha * org.x),
     double(org.xi/alpha) - double(beta/alpha * org.om),
     double(org.t) - double(beta*org.x),
     double(org.om) )
  );
}

/*
 * Output Grating
 */
inline coordinate GratingOut(coordinate org, // The original coordinate
     double alpha_orig,   // Parameter of Grating
     double beta_orig)    // Parameter of Grating
{
  double alpha = 1.0 / alpha_orig;
  double beta = 1.0 * (beta_orig / alpha_orig);
  return(GratingIn(org, alpha, beta));
}

/*
 * Spectrometer
 */
inline coordinate Spectrometer(coordinate org, // The original coordinate
       double alpha,   // Parameter of Grating
       double beta,    // Parameter of Grating
       double f,       // Focal Length of Lens
       double k)       // Transversive Wave Vector
{
  return( coordinate( -alpha*f/k*org.xi,
     k/(alpha*f)*org.x - beta/alpha*org.om,
     org.t+beta*f/k*org.xi,
     org.om )
  );
}
```



```
/*
 * 2-f system (Spatial Fourier Transform)
 */
inline coordinate TwoFsystem(coordinate org, // The original coordinate
     double f,       // Focal Length of Lens
     double k)       // Transversive Wave Vector
{
  return( coordinate( -f/k*org.xi,
     k/f*org.x,
     org.t,
     org.om )
  );
}

/*
 * Temporal Fresnel Diffraction
 */
inline coordinate TFresnel (coordinate org,
    double alpha,
    double beta,
    double k,
    double zt       // diffraction time
    )
{
  double z;
  coordinate xt;

  z =  zt;

  xt = org;
  xt = GratingOut (xt, alpha, beta);
  xt = Propagation (xt, z, k, 0.0);
  xt = GratingIn (xt, alpha, beta);

  return (xt);
}

/*
 * Temporal Fresnel Diffraction Reversal Setup
 */
inline coordinate TFresnelR (coordinate org,
    double alpha,
    double beta,
    double k,
    double zt       // diffraction time
    )
{
  double z;
  coordinate xt;
```

```
  z =  zt;

  xt = org;
  xt = GratingOut (xt, alpha, -beta);
  xt = Propagation (xt, z, k, 0.0);
  xt = GratingIn (xt, alpha, beta);

  return (xt);
}

/*
 * Temporal Fresnel Diffraction with Defocus
 */
inline coordinate TFresnelDefocus (coordinate org,
   double alpha,
   double beta,
   double k,
   double zt,       // diffraction time
   double alpha_defocus
    )
{
  double z;
  double dalpha = alpha * (1.0 -alpha_defocus);
  coordinate xt;

  z =  zt;

  xt = org;
  xt = GratingOut (xt, alpha, beta);
  xt = Propagation (xt, z, k, 0.0);
  xt = GratingIn (xt, dalpha, beta);

  return (xt);
}

/*
 * Time-Lens
 */
inline coordinate TimeLens (coordinate org,
    double pw2 // pw2: PhiW^2
    )
{
  return( coordinate( org.x,
      org.xi,
      org.t,
      org.t * pw2 + org.om ));
}

/*
```



```
 * Temporal Imaging System
 */
inline coordinate TImaging (coordinate org,
    double alpha,
    double beta,
    double k,
    double zt1,
    double zt2,
    double pw2
    )
{
  coordinate xt;

  xt = org;
  xt = TFresnel (xt, alpha, beta, k, zt2);
  xt = TimeLens (xt, pw2);
  xt = TFresnel (xt, alpha, beta, k, zt1);

  return (xt);
}

/*
 * Temporal Imaging with variout Gratings
 */
inline coordinate TImagingVG (coordinate org,
      double alpha1,
      double beta1,
      double alpha2,
      double beta2,
      double alpha3,
      double beta3,
      double alpha4,
      double beta4,
      double k,
      double zt1,
      double zt2,
      double pw2
      )
{
  coordinate xt;

  xt = org;

  xt = GratingOut (xt, alpha4, beta4);
  xt = Propagation (xt, zt2, k, 0.0);
  xt = GratingIn (xt, alpha3, beta3);

  xt = TimeLens (xt, pw2);

  xt = GratingOut (xt, alpha2, beta2);
```

```
  xt = Propagation (xt, zt1, k, 0.0);
  xt = GratingIn (xt, alpha1, beta1);

  return (xt);
}

/*
 * Temporal Imaging
 */
inline coordinate TImagingFT (coordinate org,
      double alpha,
      double beta,
      double k,
      double zt1,
      double zt2,
      double pw2,
      double ftf
    )
{
  coordinate xt;

  xt = org;
  xt = TwoFsystem(xt, ftf, k);
  xt = TFresnel (xt, alpha, beta, k, zt2);
  xt = TimeLens (xt, pw2);
  xt = TFresnel (xt, alpha, beta, k, zt1);

  return (xt);
}


/*
 * Temporal Imaging Union
 * (Represented by one coordinate transformation)
 */
inline coordinate TImagingUnion (coordinate org,
 double beta,
 double k,
 double pw2,
 double mt
 )
{
  return( coordinate(
     (2.0 * mt -1.0)*org.x
     + (1.0-mt)/beta * org.t
     + 2.0*pw2*(1.0-mt)/(beta * k) * org.om,

     4.0 * beta * beta * k / pw2 * org.x
     + (2.0/mt -1) * org.xi
     - 2.0 * beta * k / pw2 * org.t
```



```
     - 2.0 * beta * (1.0 + mt) / mt * org.om,

     -2.0 * beta * (mt+1.0) * org.x
     +2.0 * pw2 * (mt - 1.0) / (mt * beta * k) * org.xi
     + mt * org.t
     + 2.0 * pw2 * (mt - 1.0) * (mt - 1.0) / (mt * k) * org.om,

     - 2.0 * beta * k / pw2 * org.x
     + (mt - 1.0) / (beta * mt) * org.xi
     + k / pw2 * org.t
     + 1.0 / mt * org.om ));
}

/*
 * Temporal Imaging with After Propagation
 */
inline coordinate TImagingPropagation (coordinate org,
      double alpha,
      double beta,
      double k,
      double zt1,
      double zt2,
      double pw2,
      double az
      )
{
  coordinate xt;

  xt = org;
  xt = Propagation (xt, az, k, 0);
  xt = TImaging (xt, alpha, beta, k, zt1, zt2, pw2);

  return (xt);
}

/*
 * Temporal imaging with first grating tilt
 */
inline coordinate TImagingDefocus1 (coordinate org,
    double alpha,
    double beta,
    double k,
    double zt1,
    double zt2,
    double pw2,
    double alpha_defocus // [%]
    )
{
  coordinate xt;
```

```
  xt = org;
  xt = TFresnel (xt, alpha, beta, k, zt2);
  xt = TimeLens (xt, pw2);
  xt = TFresnelDefocus (xt, alpha, beta, k, zt1, alpha_defocus);

  return (xt);
}

/*
 * Temporal imaging with second grating tilt
 */
inline coordinate TImagingDefocus2 (coordinate org,
    double alpha,
    double beta,
    double k,
    double zt1,
    double zt2,
    double pw2,
    double alpha_defocus // [ 1/100 %]
    )
{
  coordinate xt;

  xt = org;
  xt = TFresnelDefocus (xt, alpha, beta, k, zt1, alpha_defocus);
  xt = TimeLens (xt, pw2);
  xt = TFresnel (xt, alpha, beta, k, zt2);

  return (xt);
}

/*
 * Temporal 4-f Imaging
 * (not verified)
 */
inline coordinate T4fImaging (coordinate org,
      double alpha,
      double beta,
      double k,
      double ft1,
      double ft2,
      double pw2_1,
      double pw2_2
      )
{
  coordinate xt;

  xt = org;

  xt = TFresnel (xt, alpha, beta, k, ft2);
```



```
  xt = TimeLens (xt, pw2_2);
  xt = TFresnel (xt, alpha, beta, k, ft2 + ft1);
  xt = TimeLens (xt, pw2_1);
  xt = TFresnel (xt, alpha, beta, k, ft1);

  return (xt);
}
```

A.2.7 WinST.h

```
/*************************************************
 *
 * The mathematical function of
 * Wigner distribution function.
 * The temporal and spatial profiles of the
 * pulse are Gaussian profiles.
 *
 *************************************************/
#include <math.h>

/*
 * Wigner distribution function of
 * singlet pulse.
 */
inline float WinSTsingle(coordinate xt){
  double result = (
   w_bias
   * exp(w_x * xt.x*xt.x)
   * exp(w_xi * xt.xi*xt.xi)
   * exp(w_t * xt.t*xt.t)
   * exp(w_om * xt.om*xt.om) );
  return( float(result) );
}

/*
 * Wigner distribution function of
 * doublet pulse
 */
inline float WinSTdouble(coordinate xt)
{
  const double tau = 150e-15; // separation of twin plus [fs]
  double result = (
   w_bias
   * exp(w_x * xt.x*xt.x)
   * exp(w_xi * xt.xi*xt.xi)
   * (exp(w_t * pow((xt.t - tau),2.0)) + exp(w_t * pow((xt.t + tau),2.0)))
   * exp(w_om * xt.om*xt.om) * pow(cos(xt.om * tau),2.0)
   );
  return( float(result) );
}
```

```
/*
 * Wrapper function for above two function.
 * You have to select one of them.
 */
inline float WinST(coordinate xt)
{
  // return( WinSTdouble(xt) ); // for singlet
  return( WinSTsingle(xt) );    // for doublet
}
```

A.2.8 CtoA.h

```
/*
 * Return the index of memory on
 * result Wigner matrix, Wst from
 * a coordinate index (i_x,i_xi,i_t,i_om).
 */
inline int CtoA(int i_x, int i_xi, int i_t, int i_om,
int NX, int NXI, int NT, int NOM){
  // N: The size of Wigner matrix.
  return( i_x*NXI*NT*NOM + i_xi*NT*NOM + i_t*NOM + i_om);
}
```

A.2.9 Ns.h

```
#ifndef __Ns_h__
#define __Ns_h__

/****************************************
 * Class containing the size of
 * Wigner matrix.
 ****************************************/
class Ns{
public:
  int X, XI, T, OM;
  /*****************************/
  Ns(int Nx, int Nxi, int Nt, int Nom){
    X  = Nx;
    XI = Nxi;
    T  = Nt;
    OM = Nom;
  }
  /*****************************/
  inline int total_size(void){ return(X*XI*T*OM); }
  /*****************************/
/*
 * Return the index of memory on
 * result Wigner matrix, Wst from
 * a coordinate index (i_x,i_xi,i_t,i_om).
```



```
 */
  inline int CtoA(int i_x, int i_xi, int i_t, int i_om){
    return( i_x*XI*T*OM + i_xi*T*OM + i_t*OM + i_om);
  }
};

#endif //__Ns_h__
```

Appendix B

List of Papers and Presentations

Papers

1. Yoshiaki Yasuno, Masahiko Mori, Masanobu Watanabe and Toyohiko Yatagai. Photon wall: Three dimensional control of femtosecond light pulse. *Proc. of SPIE*, 3491:700-703, Dec. 1998.

2. Yoshiaki Yasuno, Yasunori Sutoh, Nobukazu Yoshikawa, Msahide Itoh, Masahiko Mori, Kazuhiro Komori and and Toyohiko Yatagai. Time-space conversion of femtosecond light pulse by spatio-temporal joint transform correlator. *Opt. Commn.*, 177:135–139, Apr. 2000.

3. Yoshiaki Yasuno, Yasunori Sutoh, Masahide Itoh, Masahiko Mori and Toyohiko Yatagai. Spatio-temporal joint pulse shaper: analysis of the property by Wigner distribution function. *Proc. of SPIE*, 4089:836–841, May. 2000

4. Yoshiaki Yasuno, Motoki Nakama, Yasunori Sutoh, Masahide Itoh, Masahiko Mori and Toyohiko Yatagai. Optical coherence tomography by spectral interferometric joint transform correlator. *Optics Communications*, 186:51–56, Dec. 2000.

5. Yoshiaki Yasuno, Motoki Nakama, Yasunori Sutoh, Masahide Itoh, Masahiko Mori and Toyohiko Yatagai. Optical coherence tomography by spatio-temporal joint transform correlator. *Proc. of SPIE*, (Accepted to publication)

6. Yoshiaki Yasuno, Motoki Nakama, Yasunori Sutoh, Masahide Itoh, Masahiko Mori and Toyohiko Yatagai. Phase-resolved correlation and its application to analysis of low coherence interferogram. *Opt. Lett.*, 26(2), Jan. 2001

7. Yoshiaki Yasuno, Yasunori Sutoh, Masahide Itoh, Masahiko Mori and Toyohiko Yatagai. Analysis of Spatio-Temporally Coupled Pulse-Shaper by Wigner Distribution Function *IEICE Trans. of Electron.*, (Accepted to publication)

Collaborated Papers

1. Yasunori Sutoh, Yoshiaki Yasuno, Kenji Harada, Masahide Itoh, Masahiko Mori and Toyohiko Yatagai. Analysis of Spatio-Temporal Coupling in Femtosecond Pulse Shaper by Wigner Distribution Function, *Opt. Eng.* (Submitted)

2. 須藤泰範, 安野嘉晃, 原田建治, 伊藤雅英, 森雅彦, 谷田貝豊彦. Wigner 分布関数を用いた極短光パルスの時空間情報の解析. 光学, 29(8):502–506, 2000 年 8 月

International Presentations

1. Yoshiaki Yasuno, Masahiko Mori, Masanobu Watanabe and Toyohiko Yatagai. Femto second light pulse scanning using one-dimensional spatial light modulator. *Fourth Optoelectronics and Communications Conference*, Jul. 1998.

2. Yoshiaki Yasuno, Masahiko Mori, Masanobu Watanabe and Toyohiko Yatagai. Photon wall: Three dimensional control of femtosecond light pulse. *The Third International Conference on Applications of Photonic Technologies*, Jul. 1998.

3. Yoshiaki Yasuno, Nobukazu Yoshikiwa, Masahide Itoh, Masahiko Mori, Kazuhiro Komori, Masanobu Watanabe and Toyohiko Yatagai. Femtosecond pulseshape correlation by spatio-temporal joint transform correlator. CLEO/Pacific Rim'99, Sep. 1999.

4. Yoshiaki Yasuno, Motoki Nakama, Yasunori Sutoh, Masahide Itoh, Masahiko Mori and Toyohiko Yatagai. Optical coherence tomography by spatio-temporal joint transform correlator *International Conference on Applications of Photonic Technologies*, Jul. 2000.

5. Yoshiaki Yasuno, Yasunori Sutoh, Masahide Itoh, Masahiko Mori and Toyohiko Yatagai. Spatio-temporal joint pulse shaper - analysis of the property by Wigner distribution function -. *Optics in Computing*, Jul. 2000.

6. Yoshiaki Yasuno, Yasunori Sutoh, Masahide Ito, Masahiko Mori and Toyohiko Yatagai. Numerical analysis of spatio-temporally joint pulse shaper. *The 7th International Workshop on Femtosecond Technology*, Jul. 2000.

7. Yoshiaki Yasuno, Motoki Nakama, Yasunori Sutoh, Masahide Itoh, Masahiko Mori and Toyohiko Yatagai. Phase-resolved correlation: New technique for analysis of low coherence interferogram. *Optics in Computing*, Jan. 2001.

8. Yoshiaki Yasuno, Yasunori Sutoh, Masahide Itoh, Masahiko Mori and Toyohiko Yatagai. Numerical Analysis of Spatio-Temporal Coupling in Time Domain Microscop. *Optics in Computing*, Jan. 2001.

Domestic Presentations

1. 安野嘉晃, 森雅彦, 渡辺正信, 谷田貝豊彦. 1 次元空間光変調器を用いたフェムト秒パルス走査. 第 *45* 回応用物理学関係連合講演会. 1998 年 3 月.

2. 安野嘉晃, 森雅彦, 渡辺正信, 谷田貝豊彦. Photon wall: フェムト秒光パルスの 3 次元形状制御. 第 *59* 回応用物理学会学術講演会. 1998 年 9 月.

3. 安野嘉晃, 吉川宜一, 伊藤雅英, 森雅彦, 渡辺正信, 谷田貝豊彦. 光アドレス型液晶空間光変調器を用いた時空間パルス相関器. 第 *46* 回応用物理学関係連合講演会. 1999 年 3 月.

4. 安野嘉晃, 須藤泰範, 伊藤雅英, 森雅彦, 谷田貝豊彦. Wigner 分布関数による時空間結合パルスシェイパーの解析. 日本光学会年次学術講演会 *(Optics Japan'99)*. 1999 年 11 月.

5. 安野嘉晃, 須藤泰範, 伊藤雅英, 森雅彦, 谷田貝豊彦. 時間顕微鏡における時空間結合の解析. 第 *61* 回応用物理学会学術講演会. 2000 年 9 月.

6. 安野嘉晃, 仲間基起, 伊藤雅英, 森雅彦, 谷田貝豊彦. 位相分解相関アルゴリズムによる白色干渉信号の分解. 第 *48* 回応用物理学関係連合講演会. 2001 年 3 月.

Collabolated Presentations

1. Masahiko Mori, Yoshiaki Yasuno, Masanobu Watababe. Differentiation images on spatio-temporal plane with femtosecond light pulses. *Optics in Computing*, Jun. 1998.

2. Yasunori Sutoh, Yoshiaki Yasuno, Masahide Ito, Masahiko Mori and Toyohiko Yatagai. Analysis of spatio-temporal coupling in pulse shaper. *The 7th International Workshop on Femtosecond Technology*, Jul. 2000.

3. 仲間基起, 安野嘉晃, 伊藤雅英, 森雅彦, 谷田貝豊彦. SLD 時空間結合変換相関法によるコヒーレンストモグラフィー. 日本光学会年次学術講演会 *(Optics Japan'99)*. 1999 年 11 月.

4. 須藤泰範, 安野嘉晃, 伊藤雅英, 森雅彦, 谷田貝豊彦. 極短パルス光の時空間走査の解析. 第 *61* 回応用物理学会学術講演会. 2000 年 9 月.

5. 須藤泰範, 安野嘉晃, 伊藤雅英, 森雅彦, 谷田貝豊彦. 非線形光学結晶を用いたスペクトル干渉コヒーレンストモグラフィー. 第 *48* 回応用物理学関係連合講演会. 2001 年 3 月.

References

[1] J. W. Goodman. *Introduction to Fourier Optics.* McGraw-Hill, second edition. ISBN0-07-024254-2.

[2] A. M. Weiner, D. E. Leaird, J. S. Patel, and J. R. Wullert. *J. of Quant. Electron.*, 28(4):908–920, 1992.

[3] A. M. Weiner, D. E. Leaird, J. S. Patel, and J. R. Wullert. Programmable shaping of femtosecond optical pulses by use of 128-element liquid crystal phase modulator. *IEEE J. Quantum Electron*, 28(4):908–920, 1992.

[4] A. M. Weiner, J. P. Heritage, and J. A. Salehi. Encoding and decoding of femtosecond pulses. *Opt. Lett.*, 13:300–302, 1988.

[5] A. M. Weiner, J. P. Heritage, and E. M. Mirschner. High-resolution femtosecond pulse shaping. *J. Opt. Soc. Am. B*, 5(8):1563–1572, 1988.

[6] A. M. Weiner *et al. IEEE J. Quant. Electron*, 28:908–920, 1992.

[7] M. Takeda and K. Mutoh. Fourier transform profilometry for the automatic measurement of 3-d object shapes. *Appl. Opt.*, 22:3977–3982, 1983.

[8] J. H. Bruning, D. R. Herriott, J. E. Gallagther, D. P. Rosenfeld, A. D. White, and D. J. Brangaccio. *Appl. Opt.*, 13:2693, 1974.

[9] B. Bowe and V. Toal. White light interferometric surface profiler. *Opt. Eng.*, 37:1796–1799, 1998.

[10] H. Matsumoto and A. Hirai. A white-light interferometer using a lamp source and heterodyne detection with acousto-optic modulators. *Opt. Comm.*, 170:217–220, 1999.

[11] A. Hirai and H. Matsumoto. White-light interferometry using pseudo random-modulation for high-sensitivity and high-selectivity measurements. *Opt. Comm.*, 161:11–15, 1999.

[12] B. H. Kolner and M. Nazarathy. Temporal imaging with a time lens. *Opt. Lett.*, 14(12):630–632, 1989.

[13] E. A. Swanson. High-speed optical coherence domain reflectometry. *Opt. Lett.*, 17(2):151–153, Jan. 1992.

[14] A. C. Oliveira, F. M. M. Yasuoka, J. B. Santos, L. A. V. Carvalho, and J. C. Castro. Low-coherence lock-in interferometer for ophthalmology. *Rev. of Sci. Inst.*, 69(4):1877–1881, Apr. 1998.

[15] K. G. Larkin. Efficient nonlinear algorithm for envelope detection in white light interferometry. *J. Opt. Soc. Am. A.*, 13:832–843, 1996.

[16] N. H. Farhat and D. Psaltis. *J. Opt. Soc. Am. A*, 1:1296, 1984.

[17] D. Psaltis and N. H. Farhat. *Opt. Lett.*, 10:98–100, 1985.

[18] C. S. Weaver and J. W. Goodman. A technique for optically convolving two functions. *Appl. Opt.*, 5(7):1248–1249, 1966.

[19] A. M. Weiner. In T. Asakura, editor, *International Trends in Optics and Photonics*, 1999. (Springer-Verlag).

[20] K. Ema. Real-time ultrashort pulse shaping and pulse-shape measurement using a dynamic grating. *Japn. J. Appl. Phys.*, 30(12A):L2046–L2049, December 1991.

[21] M. C. Nuss, M. Li, T. H. Chiu, A. M. Weiner, and A. Partovi. *Opt. Lett.*, 19:664, 1994.

[22] K. Ema, M. Kuwata-Gonokami, and F. Shimizu. *Appl. Phys. Lett.*, 59:2799, 1991.

[23] Y. Yasuno *et al.* Femtosecond pulse shape correlation by spatio-temporal joint transform correlator. In *CLEO/Pacific Rim'99, Seoul, Korea*, volume 3, pages 813–814, Aug. 1999.

[24] F. Shimizu. Comperession and shaping of short light pulse. *Jpn. J. Appl. Phys.*, 26(1):L53–L55, 1987.

[25] N. Mukohzaka, N. Yoshida, H. Toyoda, Y. Kobayashi, and T. Hara. *Appl. Opt.*, 33:2804–2811, 1994.

[26] Y. Yasuno, M. Nakama, Y. Sutoh, N. Yoshikawa, M. Mori, M. Itoh, and T. Yatagai. Optical coherence tomography by spatio-temporal joint transform correlator. In *International Conference on the Application of Photonic Technology*, June 2000. (submitted).

[27] B. Javidi. *Appl. Opt.*, 28:2358–2367, 1989.

[28] J. D. Gaskill. Imaging through a randomely inhomogeneous medium by wavefront reconstruction. *J. Opt. Soc. Am.*, 58(5):600–608, May 1968.

[29] P. A. Flournoy, R. W. McClure, and G. Wyntjes. White-light interferometric thickness gauge. *Appl. Opt.*, 11(9):1907–1915, Sep. 1972.

[30] B. S. Lee and T. C. Strand. Profilometry with a coherence scanning microscope. *Appl. Opt.*, 29(26):3784–3788, Sep. 1990.

[31] B. Bowe and V. Toal. White light interferometric surface profiler. *Opt. Eng.*, 37(6):1796–1799, Jun. 1998.

[32] Jr. B. W. Colston, M. J. Everett, L. B. Da Silva, L. L. Otis, P. Stroeve, and H. Nathel. Imaging of hard- and soft-tissue structure in the oral cavity by optical coherence tomography. *Appl. Opt.*, 37(16):3582–3585, Jun. 1998.

[33] D. Meshulach, D. Yelin, and Y. Silberberg. White light dispersion measurements by one- and two-dimensional spectral interference. *J. of Quant. Electron.*, 33(11):1969–1974, Nov. 1997.

[34] R. Leitgeb, M. Wojtkowski, A. Kowalczyk, C. K. Hitzenberger, M. Sticker, and A. F. Fercher. Spectral measurment of absorption by spectroscopic frequency-domain optical coherence tomography. *Opt. Lett.*, 25:820–822, 2000.

[35] Y. Yasuno, Y. Sutoh, N. Yoshikawa a, M. Itoh, M. Mori, K. Komori, M. Watanabe, and T. Yatagai. Time-space conversion of femtosecond light pulse by spatio-temporal joint transform correlator. *Opt. Commn.*, 177:135–139, 2000.

[36] A. M. Weiner, D. E. Leaird, J. S. Patel, and J. R. Wullert. *Opt. Lett.*, 15(6):pp. 326–328, 1990.

[37] C. W. Hillegas, J. X. Tull, D. Goswami, D. Strickland, and W. S. Warren. Femtosecond laser pulse shaping by use of microsecond radio-frequency pulses. *Opt. Lett.*, 19(10):737–739, 1994.

[38] K. W. Chu and F. M. Dickey. Optical coherence multiplexing for interprocessor communications. *Opt. Engin.*, 30(3):337–344, 1991.

[39] A. Gh. Podoleanu, S. Taplin, D. J. Webb, and D. A. Jackson. Theoretical study of talbot-like bands observed using a laser diode below threshold. *J. Pure and Appl. Opt.*, 7:517–536, 1998.

[40] J. P. Goedgebuer, A. Hamel, H. Porte, and N. Butterlin. Analysis of optical crosstalk in coherence multiplexed systems employing a short coherence laser diode with arbitrary power spectrum. *IEEE J. Quantum Electron.*, 26(7):1217–1226, 1990.

[41] F. Li, N. Mukohzaka, N. Yoshida, Y. Igasaki, H. Toyoda, T. Inoue, Y. Kobayashi, and T. Hara. Phase modulation characteristics analysis of optically-addressed parallel-aligned nematic liquid crystal phase-only spatial light modulator combined with a liquid crystal display. *Opt. Rev.*, 5(3):174–178, 1998.

[42] N. Mukohzaka, N. Yoshida, H. Toyoda, Y. Kobayashi, and T. Hara. Diffraction efficiency analysis of a parallel-aligned nematic-liquid-crystal spatial light modulator. *Appl. Opt.*, 33(14):2804–2811, 1994.

[43] Y. Igasaki, N. Yoshida, H. Toyoda, Y. Kobayashi, N. Mukohzaka, and T. Hara. High speed parallel aligned liquid crystal spatial light modulator operated at 180 Hz. *Opt. Rev.*, 4(1b):167–169, 1997.

[44] S. D. Silvestri, J. G. Fujimoto, E. P. Ippen, E. B. Gamble Jr., L. R. Williams, and K. A. Nelson. Femtosecond time-resolved measurments of optic phonon dephasing by impulsive stimulatied Raman scattering in α-perylene crystal from 20 to 300 k. *Chem. Phys. Lett.*, 16:146–151, 1985.

[45] A. M. Weiner, J. P. Heritage, R. J. Hawkins, R. N. Thurston, and E. M. Kirschner. Experimental observation of the fundamental dark soliton in optical fibers. *Phys. Rev. Lett..*, 61:2445–2448, 1988.

[46] J. J. Baumberg, A. P. Heberle, K. Köhler, and K. Ploo. Ultrafast coherent carrier control in quantum wells. *J. Opt. Soc. Am. B*, 13(6):1246–1250, June 1996.

[47] M. B. Danailov and I. P. Christov. Time-space shaping of light pulses by fourier optical processing. *J. Modern Opt.*, 36:725–731, 1989.

[48] M. M. Wefers and K. A. Nelson. Space-time profiles of shaped ultrafast optical waveforms. *IEEE J. Quant. Elect.*, 32:161–172, 1996.

[49] F. Shimizu. Compression and shaping of short light pulse. *Jpn. J. Appl. Phys.*, 26:L53–L55, 1987.

[50] W. Mecklenbräuker et. al. *The Wigner Distribution.* Elsevier, 1997.

[51] M. J. Bastiaans. The Wigner distribution function applied to optical signals and systems. *Opt. Commun.*, 25(1):26–30, 1978.

[52] Y. Yasuno, M. Mori, M. Watanabe, and T. Yatagai. Photon wall: Three dimensional control of femto second light pulse. *SPIE*, 3491:700–703, 1998.

[53] Jérôme Paye and Arnold Migus. Space-time Wigner function and their application to the analysis of a pulse shaper. *J. Opt. Soc. Am. B*, 12(8):1480–1490, 1995.

[54] M. Mori, Y. Yasuno, M. Watanabe, and T. Yatagai. Differentiation images on spatio-temporal plane with femtosecond light pulses. In *Optics in Computing*, 1998. held in Brugee.

[55] C. V. Bennet, R. P. Scott, and B. H. Kolner. Temporal magnification and reversal of 100 Gb/s optical-data with an up-conversion time microscope. *Appl. Phys. Lett.*, 65(20):2513–2515, Nov. 1994.

Acknowledgement

I greatly acknowledge the supervisor of this thesis, Professor Toyohiko Yatagai and Professor Masahide Itoh, and wish to express my gratitude for important discussions of Dr. Kenji Harada, Mr. Motoki Nakama, Mr. Yasunori Sutoh, Mr. Masahito Okida and all of the members of Yatagai laboratory.

This research is partially founded by Electrotechnical laboratory and Dr. Masahiko Mori in Optoelectronics division of the laboratory provided me some helpful suggestions. This research and the author are supported by Japan Society for the Promotion of Science. I would like to thank them.

Dr. Keiichiro Kagawa, Dr. Rieko Inaba and many other young researchers in the field of optics provided me many inspirations and good discussions.

Index